

REPORT DOCUMENTATION PAGE			Form Approved OMB NO. 0704-0188	
Public Reporting burden for this collection of information is estimated to average 1 hour per response, including the time for reviewing instructions, searching existing data sources, gathering and maintaining the data needed, and completing and reviewing the collection of information. Send comment regarding this burden estimates or any other aspect of this collection of information, including suggestions for reducing this burden, to Washington Headquarters Services, Directorate for information Operations and Reports, 1215 Jefferson Davis Highway, Suite 1204, Arlington, VA 22202-4302, and to the Office of Management and Budget, Paperwork Reduction Project (0704-0188,) Washington, DC 20503.				
1. AGENCY USE ONLY (Leave Blank)		2. REPORT DATE		3. REPORT TYPE AND DATES COVERED
4. TITLE AND SUBTITLE			5. FUNDING NUMBERS	
6. AUTHOR(S)				
7. PERFORMING ORGANIZATION NAME(S) AND ADDRESS(ES)			8. PERFORMING ORGANIZATION REPORT NUMBER	
9. SPONSORING / MONITORING AGENCY NAME(S) AND ADDRESS(ES) AFOSR U. S. Army Research Office P.O. Box 12211 Research Triangle Park, NC 27709-2211 875 N. Randolph St. Suite 325 Arlington, VA 22203			10. SPONSORING / MONITORING AGENCY REPORT NUMBER	
11. SUPPLEMENTARY NOTES The views, opinions and/or findings contained in this report are those of the author(s) and should not be construed as an official Department of the Army position, policy or decision, unless so designated by other documentation.				
12 a. DISTRIBUTION / AVAILABILITY STATEMENT Approved for public release; distribution unlimited.			12 b. DISTRIBUTION CODE	
13. ABSTRACT (Maximum 200 words)				
14. SUBJECT TERMS			15. NUMBER OF PAGES	
			16. PRICE CODE	
17. SECURITY CLASSIFICATION OR REPORT UNCLASSIFIED	18. SECURITY CLASSIFICATION ON THIS PAGE UNCLASSIFIED	19. SECURITY CLASSIFICATION OF ABSTRACT UNCLASSIFIED	20. LIMITATION OF ABSTRACT UL	

NSN 7540-01-280-5500

Standard Form 298 (Rev.2-89)
Prescribed by ANSI Std. Z39-18
298-102

Enclosure 1

Period: Nov 2008-Nov2011

By

Prof. Sanjay Krishna, CHTM

Grant/Contract Title: NOVEL HETERENGINEERED DETECTORS FOR MULTI-COLOR INFRARED SENSING

Grant/Contract Number: FA9550-09-1-0231

Copies sent to:

Dr. Kitt Reinhardt
Program Manager, 4015 Wilson Blvd,
Arlington VA 22203-1954
Phone: (703) 588-1780
Marked For Contract: FA9550-0401-0396

Jennifer L Bell, AFOSR
4015 Wilson Blvd Rm 713,
Arlington VA 22203-1954
Phone: 703 696 5933 Email: Jennifer.bell@afosr.af.mil
Marked For Contract: FA9550-0401-0396

ONRRO San Diego
4520 Executive Drive Suite 300
San Diego CA 92121-3019
Marked For Contract: FA9550-07-1-0410

1.1 Overview

The Center for High Technology Materials (CHTM) at the University of New Mexico (UNM) is investigating high performance multi-color infrared (MWIR, 3-5 μm /LWIR, 8-12 μm) focal plane arrays (FPA) using InAs/GaSb/AlGaSb strain layer superlattices (SLS) with a dynamically tunable absorption edge. The first two years of this program will be aimed at investigating the optimal design for the SLS detectors through a positive feedback loop consisting of theoretical modeling of the bandstructure and transport followed by growth, fabrication and characterization of single pixel detectors. The second and third year will be focused on developing two-color FPAs based on this optimized design.

1.2 Summary of Achievements

The program has been very successful both on the technical aspects of the projects and the personnel aspects of the projects. Several publications including one in Nature and one in Nature Communications have been published using funding from this project. One doctoral student, Dr. Arezou Khoshakhlagh, has defended her PhD and is now a full time staff member at NASA Jet Propulsion Laboratory. One more student, Mr. Vince Cowan, who works at the Air Force Research Laboratory is completing his PhD on barrier devices based on Type II superlattices.

2. Technical Approach and Innovative Claims

One of unique features of InAs/GaSb SLS material system is the dependence of its effective bandgap on thickness of constituent layers. By varying thickness of InAs, GaSb, or both, the effective bandgap of InAs/GaSb SLS can be tailored from 3 μm to 30 μm thus allowing fabrication of devices with operating wavelengths spanning the entire IR region. Moreover, the strain in InAs/GaSb type-II SLS system facilitates suppression of interband tunneling¹ and Auger recombination² processes. The larger effective mass ($\sim 0.04m_0$) in SLS leads to a reduction of tunneling currents compared with MCT detectors of the same bandgap¹. By optimizing the oscillator strength in this material system, a large quantum efficiency and responsivity can be obtained. Commercial availability of low defect density substrates as well as a high degree of uniformity for III-V growth and processing over a large area also offers technological advantages for the InAs/GaSb SLS technology. Recent progress in this material system has led to very promising performance, especially at liquid nitrogen cooled temperatures^{3,4}.

In this program, two approaches have been identified for the realization of the *dynamically tunable absorption edge* in type II SL. Each of these approaches will be investigated methodically using a systematic study to realize the final goal of the program, namely a high performance two-color FPA. These two approaches are: (a) *Sequential but collocated two-color detection capabilities of type II InAsGaSb SLS detector based on an nBn design* and (b) *Simultaneous and collocated two-color detection capabilities of type II InAsGaSb SLS detector based on novel (on pBn or/and pBp) heteroengineered design*.

The effort has been focused on the optimization of the heterostructure designs of SLS detectors aimed to operate in MWIR and LWIR spectral regions; performance improvement of LWIR SLS detectors by application of effective passivation schemes; and actual demonstration of two- and three-color detection using SLS detectors. Moreover, we investigated basic properties of InAs/GaSb SLS material (background carrier concentration, optimization of growth parameters) detrimental for the effective device performance.

Optimization of heterostructure design of InAs/GaSb SLS Detectors

The novel PbIbN architecture has been proposed in order to reduce dark current components of LWIR ($\lambda_{50\% \text{ cut-off}} = 10.8 \mu\text{m}$) InAs/GaSb SLS detectors. In PbIbN detector, the electron and hole blocking barriers are placed near the P type and N type contacts, respectively. All the layers, including contacts, barrier layers and absorber layer have been designed by the use of InAs/GaSb SLS by merely changing the thicknesses of constituent layers. The PbIbN design has shown over two orders of magnitude reduction in dark current over a conventional PIN design. Details of this approach were published in the Applied Physics Letters and Infrared Physics & Technology (Gautam et al, publications 1-2 from the publication list).

Passivation of LWIR InAs/GaSb SLS Detectors

During the individual pixel isolation process of InAs/GaSb SLS FPA the periodic crystal structure terminates abruptly resulting in formation of unsatisfied (dangling) chemical bonds responsible for generation of surface states within the bandgap. Allowed energy states within the forbidden energy band-gap region of semiconductor cause pinning of the surface Fermi level near the midgap and, as a consequence, enhance the surface leakage currents. Since in order to use SLS detectors in FPAs their dimensions need to be reduced to $\sim 20\mu\text{m}$, the surface leakage currents become a dominant contributor to the dark current. Thus, in order to improve the overall device performance, methods for elimination of surface currents, i.e. passivation treatments, have to be developed for InAs/GaSb SLS material system.

We investigated various passivation techniques for LWIR InAs/GaSb SLS detectors. We showed that dielectric passivation is effective for SLS detectors operating in MWIR range, however, it does not provide sufficient effectiveness, reproducibility and long-term stability for photodiodes operating in 8-12 μm range. Moreover, band bending caused by surface states at the semiconductor-dielectric interface results in increase of surface tunneling currents. LWIR SLS detector passivation with SU-8 and electrochemically deposited sulphur (ECP) had resulted in tremendous reduction of dark current.

SU-8 is an epoxy-based negative photoresist, which was developed by IBM. Presently, SU-8 is widely used in MEMs and optoelectronics applications. SU-8 consists of a bisphenol A novolak epoxy resin, a photo initiator, and solvent γ -butyrolactone. The photo initiator is easily broken down and changes into strong acid (HCbF6) upon

exposure of UV. This acid causes a high cross-link density in the SU-8 film, thereby leading to an increase in its chemical resistance to the developer. Photo-polymerized SU-8 is mechanically and chemically stable after a hard bake. Application of SU-8 is performed at room temperature and easily integrated into device fabrication process.

The electrochemical cell for the ECP treatment consisted of the sample (anode), a platinum mesh electrode (cathode) and the electrolyte in a glass beaker at room temperature. The electrolyte was 0.1 M Na₂S in ethylene glycol. A square-shaped constant DC current with a magnitude of 33 μ A was supplied from the programmable current source to the back of the sample for a limited amount of time (5 min).

Passivation details as well as the improvement of device performance were published in Infrared Physics & Technology, Applied Physics Letters, and Journal of Electronic Materials (Kim et al, Plis et al, Kutty et al, publications 3-6 from the publication list)

Demonstration of Multicolor Detection using SLS Detectors

Despite the prominent advantages of SLS technology, only few reports of dual-band detectors based on InAs/GaSb SLS have been published so far. The dual-color SLS cameras (MWIR (4 μ m)/MWIR (5 μ m) and MWIR (7.7 μ m)/LWIR (10 μ m)) possess a vertical detector design based on two ‘back-to-back’ InAs/GaSb SLS photodiodes separated by a common ground contact layer.^{5, 6} These detectors are based on conventional p-i-n design which is characterized by high diffusion and Shockley-Read-Hall (SRH) generation-recombination dark currents. Moreover, they require multiple contacts per pixel resulting in a complicated processing scheme and expensive specific read-out circuits.

We demonstrated dual band (MWIR 5 μ m/LWIR 9 μ m) response from SLS detector with pBp architecture (Plis et al, publication 7 from the publication list) and three-color response from three contact SLS detector, which consists of SWIR, MWIR, and LWIR absorber regions separated by unipolar barriers to prevent the flow of dark carriers while allowing the flow of photogenerated carriers (Gautam et al, publications 1 and 8 from the publication list)

Basic Properties of InAs/GaSb SLS Material

One of the fundamental properties of the InAs/GaSb SLS detector absorber layer is the background carrier concentration as that determines the minority carrier lifetime and diffusion lengths, thus affecting the transport of photogenerated carriers and overall device performance. We investigated the background carrier concentration and activation energies in MWIR ($\lambda_{\text{cut-off}} \sim 5 \mu\text{m}$) and LWIR ($\lambda_{\text{cut-off}} \sim 8 \mu\text{m}$) SLS as a function of growth and measurement temperatures. Details of this study are published in Applied Physics Letters journal (Khoshakhlagh et al, publication 9 from the publication list).

The growth of the InAs/GaSb SLS was optimized for the LWIR region. Details of this approach were published in the journal of Vacuum Science and Technology (Plis et al, publication 10 from the publication list).

4. Selected publications and Conference Proceedings resulting from this work

1. N. Gautam, H.S. Kim, S. Myers, E. Plis, M. N. Kutty, M. Naydenkov, B. Klein, L.R.Dawson, S. Krishna, "Heterojunction Bandgap Engineered Photodetector Based on Type-II InAs/GaSb Superlattice for Single Color and Bicolor Infrared Detection", *Infrared Physics & Technology* (2010) **DOI:** 10.1016/j.infrared.2010.12.028
2. N. Gautam, H. S. Kim, M. N. Kutty, E. Plis, L. R. Dawson, and S. Krishna, "Performance improvement of longwave infrared photodetector based on type-II InAs/GaSb superlattices using unipolar current blocking layers", *Appl. Phys. Lett.* 96, 231107 (2010)
3. E. Plis, M.N. Kutty, S. Myers, H.S. Kim, N. Gautam, L.R. Dawson, S. Krishna, "Passivation of Long-wave Infrared InAs/GaSb Strained Layer Superlattice detectors", *Infrared Physics & Technology*(2010). **DOI:** 10.1016/j.infrared.2010.12.024
4. H. S. Kim, E. Plis, N. Gautam, S. Myers, Y. Sharma, L. R. Dawson, and S.Krishna, "Reduction of surface leakage current in InAs/GaSb strained layer long wavelength superlattice detectors using SU-8 passivation", *Appl. Phys. Lett.* 97, 143512 (2010)
5. H. S. Kim, E. Plis, A. Khoshakhlagh, S. Myers, N. Gautam, Y. D. Sharma, L.R. Dawson, S. Krishna, S. J. Lee, and S. K. Noh, "Performance improvement of InAs/GaSb strained layer superlattice detectors by reducing surface leakage currents with SU-8 passivation", *Appl. Phys. Lett.* 96, 033502(2010)
6. M. N. Kutty, E. Plis, A. Khoshakhlagh, S. Myers, N. Gautam, S. Smolev, Y. Sharma, R. Dawson, S. Krishna, S.J. Lee, and S.K. Noh. "Study of Surface Treatments on InAs/GaSb Superlattice LWIR Detectors", *J. Electron. Mater.* **DOI:** 10.1007/s11664-010-1242(2010)
7. E. A. Plis, S. S. Krishna, N. Gautam, S. Myers, and S. Krishna. "Bias Switchable Dual-Band InAs/GaSb Superlattice Detector With pBp Architecture". *IEEE Photonics Journal* 3, 234 (2011)
8. N. Gautam, M. Naydenkov, S. Myers, A. V. Barve, E. Plis, T. Rotter, L. R. Dawson, and S. Krishna "Three color infrared detector using InAs/GaSb superlattices with unipolar barriers". *Appl. Phys. Lett.* 98, 121106 (2011)
9. A. Khoshakhlagh, F. Jaeckel C. Hains J. B. Rodriguez, L. R. Dawson, K. Malloy, and S. Krishna, "Background carrier concentration in midwave and longwave InAs/GaSb type II superlattices on GaAs substrate", *Appl. Phys. Lett.* 97, 051109 (2010)
10. E. Plis, A. Khoshakhlagh, S. Myers, H. S. Kim, N. Gautam, Y. D. Sharma, and S. Krishna S. J. Lee and S. K. Noh " Molecular beam epitaxy growth and

- characterization of type-II InAs/GaSb strained layer superlattices for long-wave infrared detection”, J. Vac. Sci. Technol. B 28 (3), 085010 (2010)
11. E. Plis, S. Myers, M. N. Kuty, J. Mailfert, E. P. Smith, S. Johnson, and S. Krishna, “Lateral diffusion of minority carriers in InAsSb-based nBn detectors”, Appl. Phys. Lett 97, 123503(2010)

A representative publication is attached to this report.

-
- ¹ D. L. Smith and C. Mailhot. J. Appl. Phys. **62**, 2545 (1987)
- ² C. H. Grein, M. E. Flatte, T. C. Hasenberg, J. T. Olesberg, S. A. Anson, L. Zhang, and T. F. Boggess. J. Appl. Phys. **92**, 7311 (2002)
- ³ B. M. Nguyen, D. Hoffman, P. Y. Delaunay, and M. Razeghi, Appl. Phys. Lett. **91**, 163511 (2007).
- ⁴ D. Z.-Y. Ting, C. J. Hill, A. Soibel, S. A. Keo, J. M. Mumolo, J. Nguyen, and S. D. Gunapala, Appl. Phys. Lett. **95**, 023508 (2009)
- ⁵ R. Rehm, A. Walther, J. Fleißner, J. Schmitz, J. Ziegler, W. Cabanski, and R. Breiter, Proc. SPIE **6206**, 62060Y-1 (2006)
- ⁶ P.-Y. Delaunay, B.-M. Nguen, D. Hoffman, A. Hood, E. K.-W. Huang, M. Razeghi, and M. Tidrow. Appl. Phys. Lett. **92**, 111112 (2008)

ARTICLE

Received 5 Jan 2011 | Accepted 17 Mar 2011 | Published 19 Apr 2011

DOI: 10.1038/ncomms1283

A monolithically integrated plasmonic infrared quantum dot camera

Sang Jun Lee^{1,*}, Zahyun Ku^{2,*}, Ajit Barve², John Montoya², Woo-Yong Jang², S.R.J. Brueck², Mani Sundaram³, Axel Reisinger³, Sanjay Krishna² & Sam Kyu Noh¹

In the past few years, there has been increasing interest in surface plasmon-polaritons, as a result of the strong near-field enhancement of the electric fields at a metal-dielectric interface. Here we show the first demonstration of a monolithically integrated plasmonic focal plane array (FPA) in the mid-infrared region, using a metal with a two-dimensional hole array on top of an intersubband quantum-dots-in-a-well (DWELL) heterostructure FPA coupled to a read-out integrated circuit. Excellent infrared imagery was obtained with over a 160% increase in the ratio of the signal voltage (V_s) to the noise voltage (V_n) of the DWELL camera at the resonant wavelength of $\lambda = 6.1 \mu\text{m}$. This demonstration paves the way for the development of a new generation of pixel-level spectropolarimetric imagers, which will enable bio-inspired (for example, colour vision) infrared sensors with enhanced detectivity (D^*) or higher operating temperatures.

¹ Division of Industrial Metrology, Korea Research Institute of Standards and Science, Daejeon 305-340, Korea. ² Department of Electrical and Computer Engineering, Center for High Technology Materials, University of New Mexico, Albuquerque, New Mexico 87106, USA. ³ QmagiQ, LLC, 22 Cotton Road, Unit H, Suite 180, Nashua, New Hampshire 03063, USA. *These authors contributed equally to this work. †Present address: Air Force Research Laboratory, Wright-Patterson Air Force Base, Ohio 45433, USA. Correspondence and requests for materials should be addressed to S.K. (email: skrishna@chtm.unm.edu) or to S.K.N. (email: sknoh@kriss.re.kr).

Infrared imagers operating in the 3–12 μm range are useful for a variety of applications ranging from night vision to non-invasive medical diagnostics¹. The past decade has witnessed dramatic advances in infrared imaging technology with the introduction of new materials such as quantum dots² and superlattices³, which are posing a challenge to the 50-year incumbent technologies (HgCdTe and InSb). Focal plane array (FPA) technology has progressed from a first generation of single pixel and linear arrays (1960–70s), through a second generation of small format (128×128/256×256) 2D arrays (1980–90s) to a third generation of large format (4×4 K), dual band and higher operating temperature imagers⁴. However, to date all of the pixels in an infrared camera are as close to identical as possible, thus presenting only a ‘black and white’ version of a scene. In contrast, imagers found in nature such as the human eye encode information such as colour, dynamic range and polarization at the pixel level.

The quantum dots were grown using solid source molecular beam epitaxy (MBE) using a Stranski–Krastronow growth mode, in which strain driven dynamics drive the formation of the dots similar to the processes that lead to the self-assembly of oil droplets on a water surface⁵. In particular, the dots-in-a-well (DWELL) detector architecture pioneered at the University of New Mexico was used as a prototype in these studies^{6,7}. The DWELL architecture is a hybrid structure in which InAs quantum dots are placed in an InGaAs quantum well. The DWELLs combine the good control over the operating wavelength of quantum-well infrared photodetectors with the low dark current and normal incidence operation of quantum dot infrared photodetectors.

In the meanwhile, there has been increasing interest in the strongly enhanced electric fields in the local vicinity of a resonant coupling surface plasmon-polariton (SPP) structure such as a metal film perforated with a one-dimensional slit or two-dimensional (2D) hole array⁸. Various optoelectronic devices, such as lasers, detectors, filters and solar cells, are expected to benefit from this enhancement, which allows spectropolarimetric control over emission and detection processes^{9,10}. Various nanostructure architectures for enhanced-field couplers have

been explored in the literature, including bull’s eye, bow-tie, C-aperture and periodic inductive and capacitive arrays^{11–13}, fabricated by a wide variety of lithography techniques such as e-beam lithography, ion-beam lithography, nano-imprinting and interferometric lithography (IL)^{14–17}. For this study, we choose a 2D periodic hole array, which is easy to fabricate using IL¹⁷. These surface plasmon (SP) structures could be readily adapted into conventional FPA processing flows, as the feature sizes (1- to 3- μm) that are needed for infrared imagers are easily defined using standard optical lithography.

In this paper, we demonstrate the first monolithically integrated plasmonic camera using near field spectrally resonant coupling of the SPPs with infrared absorption in the quantum dots as an important step towards this broader, biomimetic vision of infrared imaging. Moreover, the plasmonics approach is detector agnostic and can be introduced into a standard imaging camera fabrication process using a single photolithography step.

Results

Design and fabrication of plasmonic infrared DWELL FPA.

Figure 1 shows a schematic diagram of the monolithically integrated quantum dot FPA with zoomed-in images of the heterostructure and a band diagram of the absorber, details of the SP structure and the simulated z -component of SP electric field. The absorber consists of 20 stacks of a InAs/In_{0.15}Ga_{0.85}As DWELL structure sandwiched between two n-GaAs contact layers of 200 nm (top) and 1,000 nm (bottom), respectively, and separated from the substrate by a 50 nm AlAs etch-stop barrier. After the epitaxial growth (details in Methods), the wafer was processed into a 320×256 (¼ VGA) FPA with a 30 μm pixel pitch using standard optical lithography, inductively coupled plasma etching, plasma-enhanced chemical vapour deposition of SiN_x contact metal and under-bump metal deposition. Indium bumps were deposited, the FPA was hybridized to an Indigo 9705 read-out integrated circuit (ROIC), and the substrate was removed using a series of mechanical polishing and dry etching steps ending at the 50 nm AlAs etch-stop layer. The detailed processing sequence is included in the Methods.

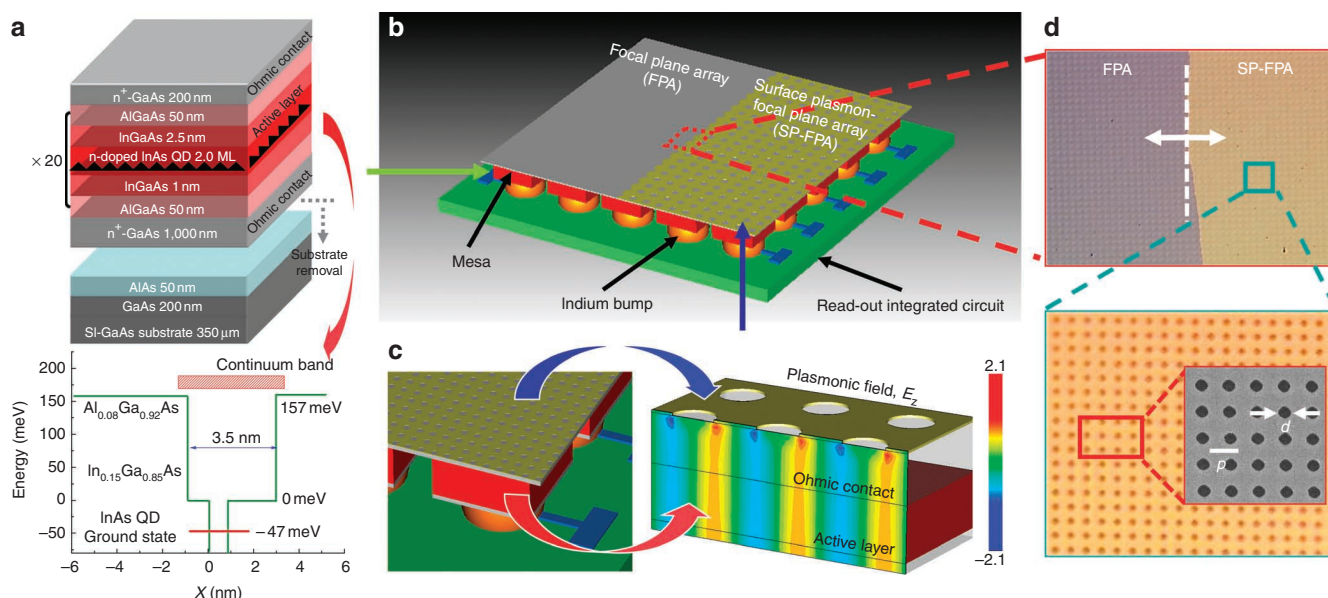


Figure 1 | Schematic of the plasmonic dots-in-a-well (DWELL) focal plane array. (a) Heterostructure schematic and band diagram of the DWELL absorber. (b) Schematic view of the surface plasmon (SP) structure defined on one half of the DWELL FPA after hybridization with a read-out integrated circuit (ROIC) and subsequent substrate removal. (c) Zoomed-in image showing the FPA bonded to the ROIC along with the SP electric field (E_z) profile. (d) Visible images of the two halves of the FPA clearly showing the non-plasmonic and plasmonic sections. The orthogonal pitches of the two-dimensional grating are both fixed at 1.79 μm (p). The metal thickness is about 50 nm. The circular aperture size (d) is fixed at 0.5 p .

Following the substrate removal, a 2D periodic SP inductive (hole) array was fabricated using IL, e-beam metal evaporation and lift-off processing. Half of the FPA was protected with a thick polymer layer during this fabrication that was later removed (see Methods for more details). A 1,000 nm bottom contact layer separated the DWELL layer from the SP array, which slightly impacts the overlap between the SPP field and the absorption region.

To determine the optimized SP structure to integrate with the FPA, a series of square symmetry 2D Ti/Au SP hole arrays were fabricated on a 1,000 nm epitaxially grown n-GaAs ($2 \times 18 \text{ cm}^{-3}$) layers with pitches ranging from 1.79 to 2.33 μm . A 2D square array of circular apertures was formed with a nominal ratio of diameter d to lattice spacing p , $d/p \sim 0.5$. The normal incidence transmission was measured using a Fourier transform infrared (FTIR) spectrometer and was normalized to the transmission through a bare substrate.

Experimental and simulated SP resonances. For normal incidence geometry, the SP resonance wavelengths are given by

$$\lambda_{i,j} = \frac{p \cdot \text{Re} \left(\sqrt{\frac{\epsilon_d \cdot \epsilon_m}{\epsilon_d + \epsilon_m}} \right)}{\sqrt{i^2 + j^2}} \quad (1)$$

where i and j are integer indices indicating the order of the coupling, p is the pitch of the SP structure, ϵ_k is the complex permittivity ($\epsilon_k = \epsilon'_k + i\epsilon''_k$, where $k = d$ (dielectric) or m (metal))^{10,13,18}. The electromagnetic field profile of the SP structure was modelled using both a finite integration technique (CST Microwave Studio, CST Studio Suite (www.cst.com)) and a rigorous coupled-wave analysis^{19,20}. The refractive index of the material (n_{eff}) was taken to be the effective index of the first order resonance of SP modes ($\sim \lambda_{1,0}/p$) and the Drude model for the gold dielectric function at frequencies of interest is described by a plasma frequency $\omega_p = 9.02 \text{ eV}$ and a scattering frequency $\omega_c = 0.027 \text{ eV}$ (refs 21, 22).

As expected, the resonance wavelengths linearly increased with the pitch. The experimentally measured resonances demonstrate very good agreement with the theoretically simulated transmission spectra, also shown in Figure 2. A pitch of 1.79 μm was chosen for the SP array for the FPA integration corresponding to a (1,0) resonance of $\sim 6.1 \mu\text{m}$ and a (1,1) resonance of $\sim 4.3 \mu\text{m}$.

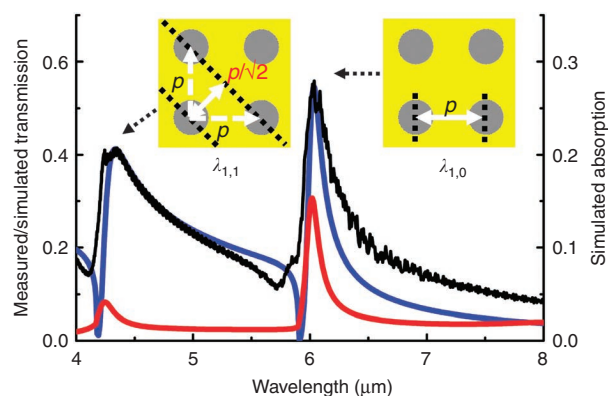


Figure 2 | Transmission spectrum of plasmonic structures. Measured transmission (black line) and simulated transmission (blue line)/absorption (red line) obtained from a 1,000 nm n-GaAs layer obtained using Fourier transform infrared (FTIR) spectrometer and rigorous coupled-wave analysis simulation showing good agreement between the experimental measurement and the theoretical calculation. The pitch corresponding to the two resonances are shown in the inset to the figure. A pitch of 1.79 μm was used in the fabrication of the SP on the DWELL FPA.

Characterization of plasmonic infrared DWELL FPA. The spectral responses of the two FPA sections (with and without the plasmonic coupler) were measured using a monochromator ($f/4$) and are shown in Figure 3a. Resonance enhancement of the response was observed at $\lambda \sim 4.3 \mu\text{m}$ and $\lambda \sim 6.1 \mu\text{m}$ and is clearly visible in the difference plot shown in Figure 3b. The simulated absorption (arbitrary units) provides a good quantitative agreement for both resonances in terms of wavelength, linewidth and relative strengths. The indicated absorption (corresponding to $n + ik$) is due to the quantum dot infrared photodetectors material; was adjusted to fit to the measurement; and provides a qualitative estimate of the propagation length along the pixel. A $k = 0.04$ corresponds to a SP absorption length of $\sim 12 \mu\text{m}$, less than the pixel linear dimension and much less than the SP ' $1/e$ ' length of $\sim 0.2 \text{ mm}$ from the metal losses alone. Figure 3c shows the image of a blackbody using $f/2.3$ optics seen through an open slot (no filter) of a filter wheel assembly. The excellent image quality is reflected in the infrared image of the hand, with temperature differences of 50 mK being captured by the plasmonic imager. A series of visual images of the resonant enhancement was obtained using narrow band filters ($\Delta\lambda = 140 \text{ nm}$) placed in front of the blackbody. Four different cases are shown in Figure 3d–g. Below the (1,1) resonance ($\lambda = 3.99 \mu\text{m}$), there is only a very small difference between the SP and the non-SP halves of the FPA. In the vicinity of the (1,1) resonance ($\lambda = 4.54 \mu\text{m}$), the SP-half of the FPA appears slightly brighter than the non-SP half of the FPA. Close to the (1,0) resonance ($\lambda = 5.95 \mu\text{m}$), there is a clear enhancement of the SP-half of the FPA. Past the (1,0) resonance ($\lambda = 6.83 \mu\text{m}$), the non-SP portion of the FPA appears brighter. These observations correlate very well with the measured spectral responses as shown in Figure 3b.

Radiometric characterization of the plasmonic FPA was undertaken using a calibrated blackbody source along with the narrow bandpass filters. Figure 4 depicts the ratio of V_s to V_n in which the enhancement is more than 160%. The difference in the enhancement factor between the measurements done with the monochromator (Fig. 3) and the narrow band pass filters (Fig. 4) could be due to the sensitivity of the measurements to the angle of incidence as the radiometric measurements were at a smaller $f/\#$ (closer to normal incidence) than the spectral measurements. The single pixel results indicate that further improvements are likely with more optimized coupling structures; normal incidence enhancements of $\times 30$ have been reported²³. This will result in a decrease in the minimum temperature difference that can be recorded by an infrared imager or to an increase in the operating temperature of the camera for the same signal to noise. This is especially important for quantum dot (QD)-based detectors, which have lower dark currents compared with quantum-well infrared photodetectors and type II strained-layer superlattices, but suffer from poor quantum efficiency. Alternatively, this allows a reduction in the active volume of superlattice detectors to reduce the dark current while retaining a high quantum efficiency. The demonstration of this performance enhancement in a full FPA format, validating the single pixel results and demonstrating the applicability to small (24 μm pixels), the absence of obvious crosstalk effects, and the applicability to realistic angular acceptances is an important step towards the integration of plasmonic structures into next generation infrared FPAs.

The present work opens up a huge optimization parameter space. Different SP structures, such as bull's eye, C-aperture and bow-tie aperture, need to be investigated and the resonant enhancement as a function of the field of view needs to be studied. Moreover, these structures can be integrated into the front side processing of the FPA, under the indium bumps, thereby enabling the fabrication of these structures at the wafer level (as opposed to the die level processing reported here). Single pixel results indicate the viability of this approach²⁴.

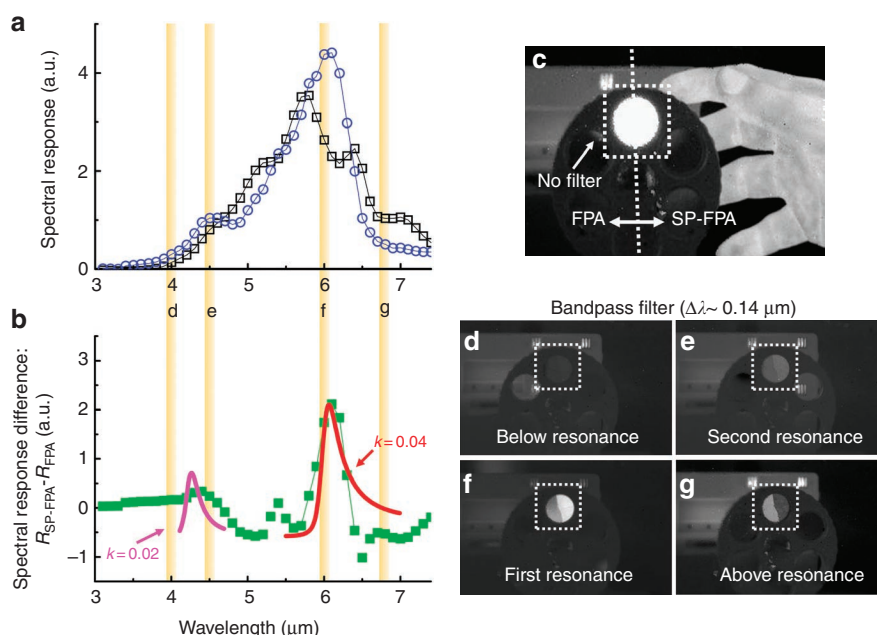


Figure 3 | Spectrally resonant enhancement in plasmonic DWELL camera. (a) Spectral response of the two halves of the plasmonic FPA using a monochromator system. Blue, spectral response of SP-FPA; black, spectral response of FPA. (b) Difference plot showing the experimentally observed peaks. The theoretically modelled (1,0) and (1,1) SP resonances are also shown using $k = 0.04$ and $k = 0.02$, respectively (k is the imaginary part of the semiconductor dielectric function dominated by the quantum dot infrared photodetector absorption). Green, difference of spectral response between SP-FPA and FPA; red (magenta), theoretically modelled first (second) order SP resonances using $k = 0.04$ (0.02). (c) Representative image of the blackbody seen through the open slot (no filter) in the filter wheel assembly. Note the clear image of the human hand clearly showing temperature differences of < 50 mK. Infrared image of the blackbody (d) below the (1,1) resonance at $\lambda = 3.99 \mu\text{m}$, (e) near the (1,1) resonance, $\lambda = 4.54 \mu\text{m}$, (f) close to the (1,0) resonance, $\lambda = 5.95 \mu\text{m}$ and (g) beyond the (1,0) and (1,1) resonances, the response of the SP-FPA is brighter than that of the non-SP-FPA, whereas the effect is reversed off resonance. This is in very good agreement with the independent spectral response measurements shown in a.

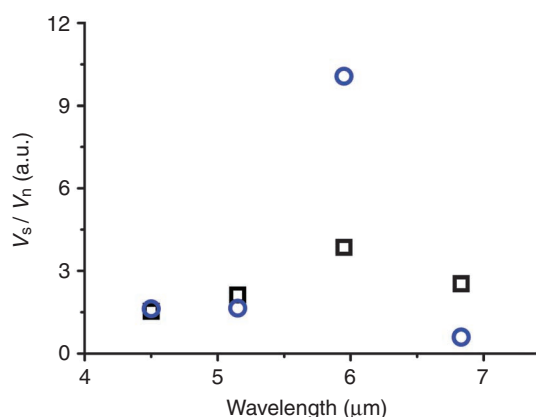


Figure 4 | Radiometric characterization of plasmonic FPA. Ratio of measured signal voltage (V_s) to noise voltage (V_n) of the detector off and on the SP resonance. The enhancement of V_s/V_n at the first order resonance is increased by over 160%, for this unoptimized structure. Blue, V_s/V_n of SP-FPA; black, V_s/V_n of FPA.

Discussion

The biggest impact of this work will be realized when plasmonic structures with different spectral, polarimetric and dynamic range structures are integrated into each pixel, thereby adding new functionality to an infrared FPA. We can combine this with efficient

on-chip compressive sensing algorithms to reduce the data volume while increasing the information from the sensor. This approach of combining a powerful multimodal sensor with ultra-efficient data compression techniques has been perfected by nature. The human eye for instance has a retina with over 150 million photoreceptors. But the amount of data that is fed into the optic nerve, which only has 1 million nerve endings, is compressed by at least 2 orders of magnitude. Scientists now believe that the retina only sends 10–12 compressed images to the brain for the reconstruction of a rich visual image with this sparse data²⁵. Thus, the human eye has the ability to sense a huge amount of multimodal data but also has the intelligence to output only a small fraction for analysis. We believe that this work enables us to get one step closer to our vision of realizing a bio-inspired spectropolarimetric sensor.

Methods

Epitaxial growth of quantum DWELL infrared photodetector. The detector structure was grown on a 2-inch semi-insulating GaAs substrate with a solid source MBE machine equipped with an As₂ cracker source. A GaAs buffer layer was grown to smooth the surface before the device layer growth. A 50-nm AlAs etch stop layer was then grown, followed by 1,000 nm n-doped GaAs bottom contact layer (Si doped, $n = 2 \times 10^{18} \text{ cm}^{-3}$). The active layer consists of 20 periods of InAs quantum dots embedded in 3.5-nm thick In_{0.15}Ga_{0.85}As-Al_{0.08}Ga_{0.92}As quantum wells, each separated by 50-nm Al_{0.08}Ga_{0.92}As barriers. InAs quantum dots were deposited at 0.053 monolayer/s growth rate at 470 °C substrate temperature. The substrate temperature was ramped to 590 °C for the growth of Al_{0.08}Ga_{0.92}As barrier layers and GaAs contact layers. The growth rates, substrate temperatures and the flux ratios were previously optimized²⁶ for maximizing the photoluminescence intensity from the quantum dots. Quantum dots were n-doped with Si with approximately two electrons per dot, for optimizing²⁷ the detector performance. The thickness and compositions of In_{0.15}Ga_{0.85}As and Al_{0.08}Ga_{0.92}As layers were selected to achieve

broadband detector response with bound to continuum type of transitions. The single pixel characterization of these detectors has been previously published²⁸. The room temperature photoluminescence data obtained with He-Ne laser excitation are plotted in Supplementary Figure S1.

Fabrication of the plasmonic hybrid FPA chip. The processing scheme of the plasmonic FPA chip consists of a dry etch to form the mesa, surface passivation, ohmic metal evaporation, under bump metallization, indium deposition and indium reflow processes as shown in Supplementary Figure S2a–g. A 320×256 array mesa with a single pixel area of 24×24 μm² and 30 μm pitch was formed using standard optical lithography, inductively coupled plasma etching by BCl₃ gas. A 200-nm thick Si₃N₄ was deposited for surface passivation using plasma-enhanced chemical vapour deposition. After making a through the Si₃N₄, the ohmic contact metals of Ge(280 Å)/Au(540 Å)/Ni(200 Å)/Au(3,000 Å) were deposited by e-beam evaporation, and a rapid thermal anneal (RTA) was performed. This was followed by under bump metallization of Ti(300 Å)/Ni(1,500 Å)/Au(500 Å) and indium deposition of 3 μm thickness. After this, the deposited indium was reflowed to form indium bumps with a height over 8 μm using flux (TAC Flux 019: Indium). The fabricated FPA devices were subsequently hybridized with an Indigo 9705 silicon ROIC chip through a standard flip-chip bonding process at 170 °C using a flip chip bonder (FC150: SUSS MicroTec). To provide mechanical support between FPA and ROIC, underfill epoxy was injected between the FPA and ROIC with the aid of the capillary force as shown in Supplementary Figure S3h,i. The entire substrate was removed and a plasmonic structure was defined on ½ of the back-side of the epilayer, that is, on the top-side of hybrid FPA chip (Supplementary Fig. S2j). The GaAs substrate of 350 μm thickness was removed using a series of mechanical polishing and selective dry etching using BCl₃/SF₆ gases to a 50 nm AlAs etch stop layer. Once the substrate was removed up to the etch stop layer, the AlAs etch stop layer was removed with a hydrofluoric acid solution. Following substrate removal, half of the FPA was covered with a sacrificial photoresist (PR) layer and a periodic 2D square hole SP array was fabricated using IL to define the 2D square symmetry hole array along with e-beam metal evaporation and lift-off processing (details in Supplementary Information: SP structure fabricated by interferometric lithography) as shown in Supplementary Figure S2k. The SP metal consisting of Ti(5 nm)/Au(45 nm) was evaporated (Supplementary Fig. S2l). Supplementary Figure S3 shows the schematic, visible and SEM images of various stages of the fabrication processes. The fabricated plasmonic FPA is shown in Supplementary Figure S3c.

Surface plasmon structure fabricated by interferometric lithography. The processing steps to fabricate the SP structure with circular apertures are as follows. (I) A positive-tone PR (SPR 505A: Shipley) was spin-deposited at 4000 r.p.m. for 30 s and oven-baked at 95 °C for 3 min. (II) IL using a 355-nm 3rd YAG:Nd³⁺ laser source was carried out to produce a periodic circular hole pattern in the PR layer with two successive orthogonal one-dimensional exposures with power 50 mJ and same doses to provide a symmetrical aperture shape; a 1 min post-bake at 110 °C was used; the exposed and post-baked sample was developed (MF-702: Shipley) for 1 min and rinsed with deionized water as shown in Supplementary Figure S4a. (III) After the PR pattern was defined, consecutive e-beam evaporations were used to deposit a 5-nm thick layer of titanium (Ti) as an adhesion layer on the developed sample and a 45-nm thick layer of gold (Au) at a pressure of the order of 10^{−7} Torr during deposition and ~0.02 nm s^{−1}, followed by a lift-off processing with a acetone to remove the PR layer as shown in Supplementary Figure S4b²⁹.

FTIR transmission measurement and simulation based on a finite integration technique. To find the optimized SP structure for integration with the FPA, SP structures with various pitches (that is, $p = 1.79, 1.89, 2.0, 2.08$ and $2.33 \mu\text{m}$) were fabricated on substrate consisting of a 1 μm thick n-type GaAs layer ($2 \times 10^{18} \text{ cm}^{-3}$) grown on a semi-insulating GaAs wafer by MBE. A 2D square array of circular holes was formed with a ~1:1 line/space ratio). IL was used to fabricate large area ($1.5 \times 1.5 \text{ cm}^2$), uniform samples and making sample characterization convenient³⁰ as described above. The transmission was recorded with a Nicolet FTIR spectrometer with a KBr beam splitter and a DTGS-KBr detector. The linear transmission spectra were measured at a normal incidence and normalized to the transmission through a bare substrate as shown in Supplementary Figure S5a. In case of symmetric SP structure with circular apertures, an unpolarized FTIR beam was used to measure the transmission. The wavelength of the first order SP resonance is given by

$$\lambda_{1,0} \sim p \cdot \text{Re} \left(\frac{\epsilon_d \cdot \epsilon_m}{\sqrt{\epsilon_d + \epsilon_m}} \right) \quad (2)$$

This result can be simplified to $\lambda_{1,0} \approx p\sqrt{\epsilon_d}$ as to $|\epsilon_m| \gg \epsilon_d', \epsilon_d'', \epsilon_m'$ and $\epsilon_d'' \gg \epsilon_m''$ as shown in Supplementary Figure S5b. In addition, a finite integration technique (CST Microwave Studio) was used to obtain the electromagnetic field distribution resulting from the SP structure as shown in Supplementary Figure S5c. Both perfect electric conductor and perfect magnetic conductor boundary conditions were used to stimulate transverse electromagnetic plane wave propagating between unit cells.

Characterization of plasmonic infrared DWELL camera. The hybrid FPA was mounted in a pour-fill Dewar and cooled down to liquid nitrogen temperature at 77 K. The FPA was connected to a commercial CamiRa FPA demonstration system manufactured by SE-IR Corporation using $f/2.3$ optics. This system controls the clock, the synchronizations (frame and line) and the FPA bias voltages and interfaces to the hybridized ROIC. The ROIC reads the pixels (the image data) and sends the outputs serially to a computer port. The computer interfaced to this system performs the data processing and storage. With this setup, the spectral responses of FPA and SP-FPA were measured at the bias of 0.3 V as a monochromatic light provided by a PIActon Spectra Pro 2150i monochromator ($f/4$ optics) was tuned from 3 to 8 μm in a step of 0.1 μm. The entire test setup for FPA spectral measurement is illustrated in Supplementary Figure S6. At each wavelength, the FPA output was stored and averaged over 30 frames. Based on the measured spectra of FPA and SP-FPA, the visual demonstration was conducted by placing a filter wheel in front of an OMEGA blackbody source at 150 °C. A filter wheel consists of four narrowband optical filters with centre wavelengths at 3.99, 4.54, 5.95 and 6.83 μm and a bandwidth ($\Delta\lambda$) of 140 nm. A total of five different images were captured and displayed for cases of no filter and four different filters to visually inspect the effect of SP-FPA as compared with FPA. For a radiometric characterization of SP-FPA, the device sensitivity^{31–33} was considered and obtained by taking the ratio of the signal voltage (V_s) to the noise voltage (V_n). The V_s was measured by the FPA camera system seen the calibrated blackbody source through the narrowband filter with $\Delta\lambda \sim 140 \text{ nm}$ as shown in Supplementary Figure S7. The measurement was performed for four different wavelengths (4.54, 5.15, 5.95 and 6.83 μm). For each measurement, the corresponding temporal noise voltage V_n was obtained by computing the standard deviation of the V_s over 30 frames.

References

- Hutchinson, L. Imaging: digital infrared breast scan shows promise for detecting cancer. *Nat. Rev. Clin. Oncol.* **7**, 483 (2010).
- Krishna, S., Gunapala, S. D., Bandara, S. V., Hill, C. & Ting, D. Quantum dot based infrared focal plane arrays. *Proc. IEEE* **95**, 1838–1852 (2007).
- Hill, C. J., Soibel, A., Keo, S. A., Mumolo, J. M., Ting, D. Z. & Gunapala, S. D. Demonstration of large format mid-wavelength infrared focal plane arrays based on superlattice and BIRD detector structures. *Infrared Phys. Tech.* **52**, 348–352 (2009).
- Rogalski, A., Antoszewski, J. & Faraone, L. Third-generation infrared photodetector arrays. *J. Appl. Phys.* **105**, 091101 (2009).
- Stranski, I. N. & Krastanov, L. *Sitzungsberichte d. Akad. D. Wissenschaften in Wien. Abt. IIb* **146**, 797–810 (1937).
- Liu, G. T. The influence of quantum-well composition on the performance of quantum dot lasers using InAs/InGaAs dots-in-a-well (DWELL) structures. *IEEE J. Quantum Electron.* **36**, 1272–1279 (2000).
- Raghavan, S. *et al.* High-responsivity, normal-incidence long-wave infrared ($\lambda \sim 7.2 \mu\text{m}$) InAs/In_{0.15}Ga_{0.85}As dots-in-a-well detector. *Appl. Phys. Lett.* **81**, 1369–1371 (2002).
- Ebbesen, T. W., Lezec, H. J., Ghaemi, H. F., Thio, T. & Wolff, P. A. Extraordinary optical transmission through subwavelength hole arrays. *Nature* **391**, 667–669 (1998).
- Xu, T., Wu, Y.-K., Luo, X. & Guo, L. J. Plasmonic nanoresonators for high-resolution colour filtering and spectral image. *Nat. Commun.* **1**, 59 (2010).
- Genet, C. & Ebbesen, T. W. Light in tiny holes. *Nature* **445**, 39–46 (2007).
- Lezec, H. J. *et al.* Beaming light from a subwavelength aperture. *Science* **297**, 820–822 (2002).
- Martin-Moreno, L. *et al.* Theory of extraordinary optical transmission through subwavelength hole arrays. *Phys. Rev. Lett.* **86**, 1114–1117 (2001).
- Barnes, W. L., Dereux, A. & Ebbesen, T. W. Surface plasmon subwavelength optics. *Nature* **424**, 824–830 (2003).
- Groves, T. R., Pickard, D., Rafferty, B., Crosland, N., Adam, D. & Schubert, G. Maskless electron beam lithography: prospects, progress, and challenges. *Microelectron. Engr.* **61**, 285–293 (2002).
- Tseng, A. A., Notariacomo, A. & Chen, T. P. Nanofabrication by scanning probe microscope lithography: a review. *J. Vac. Sci. Technol. B* **23**, 877 (2005).
- Guo, L. J. Nanoimprint lithography: methods and material requirements. *Adv. Mater.* **19**, 495–513 (2007).
- Brueck, S. R. J. Optical and interferometric lithography-nanotechnology enablers. *Proc. IEEE* **93**, 1704–1721 (2005).
- Shaner, E. A., Cederberg, J. G. & Wasserman, D. Electrically tunable extraordinary optical transmission gratings. *Appl. Phys. Lett.* **91**, 181110 (2007).
- Moharam, M. G. & Gaylord, T. K. Rigorous coupled-wave analysis of planar-grating diffraction. *J. Opt. Soc. Am.* **71**, 811–818 (1981).
- Minhas, B. K., Fan, W., Agi, K., Brueck, S. R. J. & Malloy, K. J. Metallic inductive and capacitive grids: theory and experiment. *J. Opt. Soc. Am. A* **19**, 1352–1359 (2002).
- Rosenberg, J., Shenoi, R. V., Krishna, S. & Painter, O. Design of plasmonic photonic crystal resonant cavities for polarization sensitive infrared photodetectors. *Opt. Exp.* **18**, 3672–3686 (2010).
- Ordal, M. A. *et al.* Optical properties of the metals Al, Co, Cu, Au, Fe, Pb, Ni, Pd, Pt, Ag, Ti and W in the infrared and far infrared. *Appl. Opt.* **22**, 1099–1120 (1983).

23. Lee, S. C., Krishna, S. & Brueck, S. R. J. Quantum dot infrared photodetector enhanced by surface plasmon wave excitation. *Opt. Exp.* **17**, 23160–23168 (2009).
24. Lee, S. C., Krishna, S. & Brueck, S. R. J. Light direction-dependent plasmonic enhancement in quantum dot infrared photodetectors. *Appl. Phys. Lett.* **97**, 021112 (2010).
25. Roska, B. & Werblin, F. S. Vertical interactions across ten parallel stacked representations in the mammalian retina. *Nature* **410**, 583–587 (2001).
26. Stintz, A., Liu, G. T., Gray, A. L., Spillers, R., Delgado, S. M. & Malloy, K. J. Characterization of InAs quantum dots in strained $\text{In}_x\text{Ga}_{1-x}\text{As}$ quantum wells. *J. Vac. Sci. Technol. B* **18**, 1496–1501 (2000).
27. Attaluri, R. S., Annamalai, S., Posani, K. T., Stintz, A. & Krishna, S. Effects of Si doping on normal incidence InAs/ $\text{In}_{0.15}\text{Ga}_{0.85}\text{As}$ dots-in-well quantum dot infrared photodetectors. *J. Appl. Phys.* **99**, 083105 (2006).
28. Barve, A. V., Rotter, T., Sharma, Y., Lee, S., Noh, S. & Krishna, S. Systematic study of different transitions in high operating temperature quantum dots in a well photodetectors. *Appl. Phys. Lett.* **97**, 061105 (2010).
29. Xia, D., Ku, Z., Lee, S. C. & Brueck, S. R. J. Nanostructures and functional materials fabricated by interferometric lithography. *Adv. Mater.* **23**, 147–179 (2011).
30. Ku, Z. & Brueck, S. R. J. Comparison of negative refractive index materials with circular, elliptical and rectangular holes. *Opt. Exp.* **15**, 4515–4522 (2007).
31. Gunapala, S. D. *et al.* 640×512 pixels long-wavelength infrared (LWIR) quantum dot infrared photodetector (QDIP) imaging focal plane array. *IEEE J. Quantum Electron.* **43**, 230–237 (2007).
32. Vandervelde, T. E. *et al.* Quantum dots-in-a-well focal plane arrays. *IEEE J. Sel. Top. Quantum Electron.* **14**, 1150–1161 (2008).
33. Andrews, J. *et al.* Demonstration of a bias tunable quantum dots in a well focal plane array. *Infrared Phys. Tech.* **52**, 380–384 (2009).

Acknowledgments

This work was partially funded by KRISS-UNM Global Research Laboratory program (No. 2007-00011) of the National Research Foundation (NRF) of Korea. We acknowledge AFRL contract FA9453-07-C-0171 and AFOSR contract FA9550-09-1-0202. We also thank B. Klein for FTIR transmission measurements, J.O. Kim and J.W. Choe for growth of the GaAs samples for SP structure, Y.D. Sharma, S.C. Lee and R. Shenoi for technical discussions.

Author contributions

S.J.L., S.K.N. and S.K. designed the experiments. S.J.L., Z.K., A.B., J.M. and W.-Y.J. carried out the experiments. Z.K. and S.R.J.B. performed IL to fabricate the SP structure and undertook FIT/rigorous coupled-wave analysis simulations. A.R. and M.S. undertook substrate removal for the definition of the SPP. S.J.L., Z.K., A.B. and S.K. contributed to analysing the data. S.J.L., Z.K., S.R.J.B. and S.K. wrote the paper and all authors provided feedback.

Additional information

Supplementary Information accompanies this paper at <http://www.nature.com/naturecommunications>

Competing financial interests: The authors declare no competing financial interests.

Reprints and permission information is available online at <http://npg.nature.com/reprintsandpermissions/>

How to cite this article: Lee, S. J. *et al.* A monolithically integrated plasmonic infrared quantum dot camera. *Nat. Commun.* **2**:286 doi: 10.1038/ncomms1283 (2011).

Performance improvement of InAs/GaSb strained layer superlattice detectors by reducing surface leakage currents with SU-8 passivation

H. S. Kim (김하술),¹ E. Plis,¹ A. Khoshakhlagh,¹ S. Myers,¹ N. Gautam,¹ Y. D. Sharma,¹ L. R. Dawson,¹ S. Krishna,^{1,a)} S. J. Lee,² and S. K. Noh²

¹Department of Electrical and Computer Engineering, Center for High Technology Materials, University of New Mexico, Albuquerque, New Mexico 87106, USA

²Korea Research Institute of Standards and Science, Daejeon 305-340, Republic of Korea

(Received 24 September 2009; accepted 18 November 2009; published online 21 January 2010)

We report on SU-8 passivation for performance improvement of type-II InAs/GaSb strained layer superlattice detectors ($\lambda_{\text{cut-off}} \sim 4.6 \mu\text{m}$). Optical and electrical behavior of SU-8 passivated and unpassivated devices was compared. The dark current density was improved by four orders of magnitude for passivated single diodes at 77 K. The zero bias responsivity and detectivity at 77 K was equal to 0.9 A/W and 3.5×10^{12} Jones for SU-8 passivated single pixel diodes. FPA size diodes ($24 \times 24 \mu\text{m}^2$) were also fabricated and they showed responsivity and detectivity of 1.3 A/W and 3.5×10^{12} Jones, respectively at 77 K. © 2010 American Institute of Physics.

[doi:10.1063/1.3275711]

Photodiodes based on type-II InAs/GaSb strained layer superlattice (SLS) operating in the mid-wave infrared (MWIR) and long-wave infrared (LWIR) spectrum can be used in a variety of civil and military applications. Presently, the most common detectors for these applications are mercury cadmium telluride (MCT) detectors. However, MCT alloys have a small electron effective mass ($\sim 0.009 m_0$) resulting in excessive dark current due to tunneling. Moreover, lack of spatial uniformity over large areas is still an issue for MCT devices.¹ Type-II InAs/GaSb SLS offers potential advantages for the realization of high performance detectors and large-format focal plane arrays (FPAs) due to reduced Auger recombination rates, higher effective mass ($\sim 0.04 m_0$),² and favorable spatial uniformity over large areas.

One of the issues not very well understood for the SLS is the surface passivation. Generally, the device performance of small area diodes is more susceptible to surface effects than larger size device with the same geometry due to a larger perimeter-to-area ratio (P/A). Surface leakage currents are generated on the sidewalls of devices due to the abrupt termination of the crystal structure, dangling bonds, inversion layer, and interfacial traps at the device/air interface. To overcome this problem, stable and wavelength independent passivation schemes need to be developed.

Ideal passivation of InAs/GaSb SLS detectors prevents the formation of native oxides on the etched detector sidewalls, and satisfies the dangling bonds that could lead to surface states. Several passivation methods have been proposed such as chalcogenide treatment (modification of surface by sulfur atoms),³ overgrowth with larger bandgap material,⁴ and encapsulation of device sidewalls with silicon dioxide⁵ or a polyimide layer.⁶ Sulfur passivation involves the replacement of oxygen by sulfur, resulting in the formation of an ordered layer of sulfur atoms on the surface. However, temporal instability of such a passivation layer has been reported.⁷ The passivation with large bandgap material has

also been reported but this significantly complicates the FPA fabrication process. Encapsulation with silicon dioxide results in increased surface resistance by an order of magnitude. However, SiO_2 film deposition utilizes a plasma enhanced chemical vapor deposition process conducted at high temperatures. Exposure of SLS material to high temperatures could degrade the overall device performance.

In this letter, we report the use of SU-8 as a passivation material for MWIR InAs/GaSb SLS detectors and FPAs. SU-8 is a high contrast negative photoresist widely used for micromachining⁸ and optoelectronic applications⁹ for the realization of high aspect ratio structures. SU-8 contains bisphenol, a novolac epoxy resin, and photoacid generator, as the curing agent.¹⁰ Upon UV exposure, a strong acid (HCbF_6) is generated which causes the epoxy resin to form a solid structure with a high cross-linking density. Thus, photopolymerized resist shows outstanding chemical and physical robustness. SU-8 can be spin-coated on a wide range of substrates that give rise to film thicknesses in the range of 0.2–100 μm . Also, it can be easily integrated into the detector fabrication process. It is hypothesized that SU-8 is a good candidate for passivation of InAs/GaSb SLS detectors. However, no application of SU-8 for InAs/GaSb passivation has been reported so far.

The devices presented in this work are InAs/GaSb SLS photovoltaic detectors grown on Te-doped epitaxially (100) GaSb substrate by solid source MBE VG-80 system. This photodiode is based on a p-i-n design consisting of 75 periods, eight monolayers (MLs) InAs:Si ($n=4 \times 10^{18} \text{ cm}^{-3}$)/8 MLs GaSb as the bottom contact layer. This was followed by 30 periods of 8 MLs InAs:Si ($n=1 \times 10^{18} \text{ cm}^{-3}$)/8 MLs GaSb. Then 260 periods of nonintentionally doped absorber layer were grown, followed by 30 periods of 8 MLs InAs:Be ($p=1 \times 10^{18} \text{ cm}^{-3}$)/8 MLs GaSb. The structure was terminated by 20 periods of 8 MLs InAs:Be ($p=4 \times 10^{18} \text{ cm}^{-3}$)/8 MLs GaSb which formed a p-type top contact layer. In order to improve transport of minority carriers in detector structure, ten periods of SLS layers with gradually changed doping were added between the absorber and contact layers.

^{a)}Author to whom correspondence should be addressed. Electronic mail: skrishna@chtm.unm.edu.

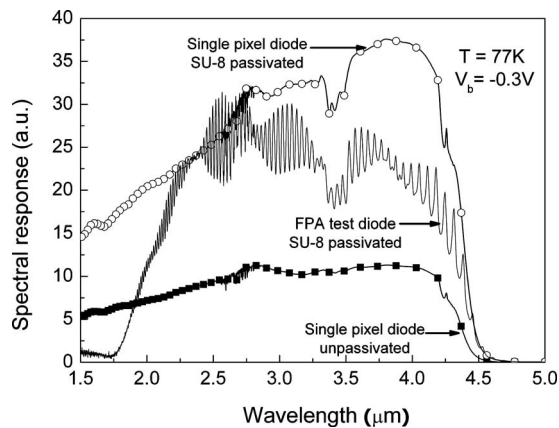


FIG. 1. Spectral response of unpassivated and SU-8 passivated single pixel diodes along with SU-8 passivated FPA test diode measured at 77 K. From the Fabry-Perot oscillation in the FPA diode, the residual GaSb thickness was found to be $\sim 36 \mu\text{m}$.

Normal incidence single pixel photodiodes with $410 \times 410 \mu\text{m}^2$ mesa area having apertures ranging from $25\text{--}300 \mu\text{m}$ were fabricated along with a variable area diode array (VADA) consisting of diodes with mesa areas ranging from 50×50 to $400 \times 400 \mu\text{m}^2$. Processing was initiated by photolithography and mesa definition etching which was performed using an inductively coupled plasma (ICP) reactor with BCl_3 gas. We use a PlasmaTherm SLR 770 ICP Chlorine Etcher with ICP power of 499 W, average rf power of 156 W, pressure of 3.2 mTorr, dc bias of 252 V, with BCl_3 flow of 30.2 SCCM at 25°C temperature. Subsequently, an ohmic contact was made by depositing Ti/Pt/Au on the bottom and top contact layers of the detectors. After contact metallization, the fabricated devices were wire bonded to a leadless chip carrier for further characterization. The rest of the fabricated devices were dipped in a $\text{H}_3\text{PO}_4:\text{H}_2\text{O}_2:\text{H}_2\text{O} = 1:2:20$ solution to remove the native oxide film on the etched mesa sidewalls and were then covered with SU-8 ($\sim 1.5 \mu\text{m}$ thickness) to act as the passivation layer.

FPA were fabricated utilizing a similar processing scheme. Each processed FPA die consists of 320×256 pixels with a $30 \mu\text{m}$ pitch. Four additional test pixels with an area of $24 \times 24 \mu\text{m}^2$ are located at the boundary of the 320×256 FPA which is used for dark current, spectral response, and noise measurements. Sidewalls of etched mesas were covered with SU-8 for passivation purposes. The FPAs were then hybridized to ISC 9705 read-out integrated circuits made by indigo using indium bump technique. To minimize thermal stress under low temperature and to reduce free carrier absorption from the GaSb substrate, the substrate was thinned using chemical mechanical polishing.

Spectral response measurements of single pixel detectors were performed using a Fourier transform IR spectrometer and a Keithley 428 preamplifier. Figure 1 shows the spectral response of the unpassivated single pixel detector (with aperture of $300 \mu\text{m}$), the SU-8 passivated single pixel detector with the same aperture, and the passivated FPA test diode at 77 K. It should be noted the single pixel devices were tested under front side illumination and FPA diode was tested under back side illumination. The zero-response cut-off wavelength for all tested detectors was equal to $\sim 4.6 \mu\text{m}$. The high frequency spectral response modulation of the FPA test pixel is attributed to the multiple interferences originated from the Fabry-Perot interference patterns caused by the residual

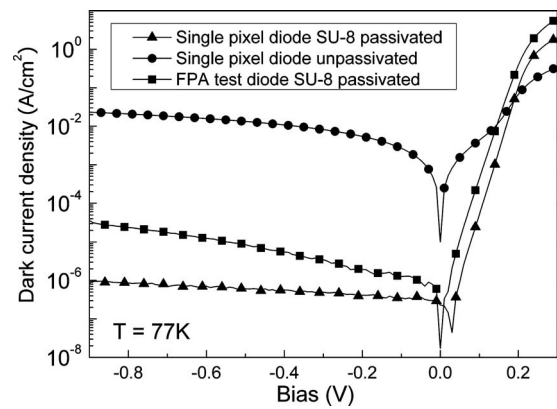


FIG. 2. Dark current density vs applied bias of unpassivated and SU-8 passivated single pixel diodes along with SU-8 passivated FPA test diode measured at 77 K.

thickness $\sim 36 \mu\text{m}$ of the unpolished substrate.

Figure 2 shows the bias dependent dark current densities for the unpassivated and passivated single pixel detectors as well as passivated FPA test diode measured at 77 K. Single-pixel passivated detector demonstrated four orders of magnitude reduction in dark current density compared with an unpassivated one (from $\sim 8 \times 10^{-3}$ to $\sim 5 \times 10^{-7} \text{ A/cm}^2$) at the same value of applied bias ($V_b = -0.3 \text{ V}$). The dark current density of passivated FPA test diode was equal to $\sim 3 \times 10^{-6} \text{ A/cm}^2$, which is approximately a factor of seven times higher than the dark current density measured on the passivated single pixel detector ($\sim 5 \times 10^{-7} \text{ A/cm}^2$) at the same value of applied bias ($V_b = -0.3 \text{ V}$). We attribute this degradation due to the additional steps in FPA fabrication, particularly, the indium reflow process, hybridization, the epoxy underfill process and mechanical thinning of the substrate, which induces a lot of stress on the FPA. However, the demonstrated level of FPA dark current is sufficient for FPA imaging¹¹ and indicates that SU-8 is a promising material for FPA passivation.

To illustrate the relationship between the temperature and dark current, the dark current density at -0.3 V is plotted as a function of inverse temperature in Fig. 3. The un-

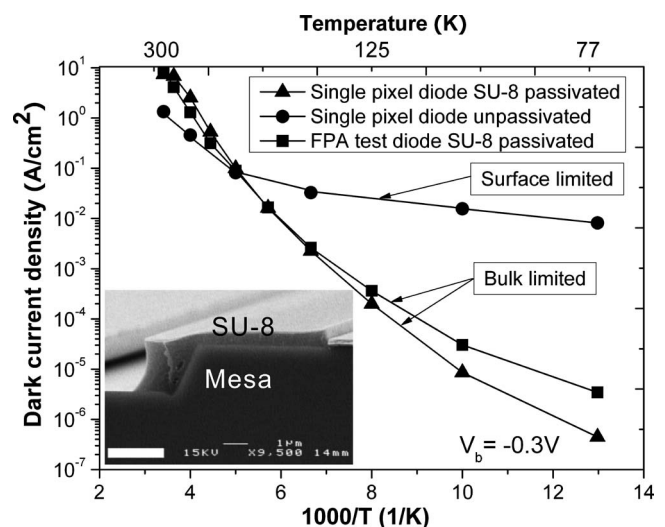


FIG. 3. Temperature dependent dark current density for unpassivated and SU-8 passivated single pixel diodes along with SU-8 passivated FPA test diode measured at 77 K. Inset shows the detector mesa sidewall encapsulated by SU-8 with a thickness of approximately $\sim 1.5 \mu\text{m}$.

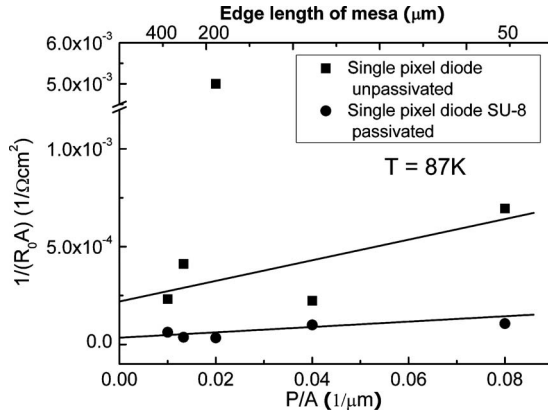


FIG. 4. The dependence of dynamic resistance-area product at zero bias vs (P/A) ratio for variable area diodes passivated by SU-8 at 87 K.

passivated device shows a higher surface leakage current density than the passivated device at low temperatures. On the contrary, SU-8 passivated devices follow an Arrhenius type behavior at high temperature, indicating that the dominant dark current mechanism is bulk limited diffusion. The calculated activation energy of the FPA test pixel is equal to 0.245 eV which is close to the expected value of the device bandgap. The inset to Fig. 3 shows a $410 \times 410 \mu\text{m}^2$ mesa covered with $\sim 1.5 \mu\text{m}$ thick SU-8 layer.

The effectiveness of SU-8 passivation was evaluated using the VADA technique.¹² The inverse of the dynamic resistance-area product (R_0A) at zero bias as a function of the perimeter to area ratio at 87 K for passivated diodes is shown in Fig. 4. The surface dependence of R_0A can be approximated as

$$1/R_0A = [(1/R_0A)_{\text{bulk}} + (1/r_{\text{surface}}) \times (P/A)], \quad (1)$$

where $(R_0A)_{\text{bulk}}$ is the bulk R_0A contribution ($\Omega \text{ cm}^2$), r_{surface} is the surface resistivity ($\Omega \text{ cm}$), P is the diode's perimeter, and A is the diode's area. The slope of the function given by Eq. (1) is directly proportional to the surface-dependent leakage current of the diode. We found values of r_{surface} equal to $\sim 1.9 \times 10^2$ and $\sim 1.0 \times 10^3 \Omega \text{ cm}$, for the unpassivated and the SU-8 passivated single pixel device, respectively, leading to a fivefold increase in the surface resistivity at 87 K.

The responsivity of both the single pixel detector and the FPA test diode passivated with SU-8 was measured under $f/2$ illumination using a calibrated blackbody source at 800 °C. The zero bias responsivity at $4 \mu\text{m}$ was equal to 0.9 and 1.3 A/W for the passivated single pixel diode and FPA test diode, respectively, as shown in Fig. 5(a). We attribute the larger responsivity due to the double path configuration of the FPA. The peak D^* , shown in Fig. 5(b), was equal to $\sim 3.5 \times 10^{12}$ Jones for the passivated single pixel detector and $\sim 3.45 \times 10^{12}$ Jones for the FPA test diode at $4.0 \mu\text{m}$ and 77 K under zero bias.

In conclusion, we have demonstrated improved performance of MWIR ($\lambda_{\text{cut-off}} \sim 4.6 \mu\text{m}$) single pixel detectors with p-i-n design and FPAs based on InAs/GaSb SLS with SU-8 passivation. Comparison of unpassivated and SU-8 passivated single pixel devices at 77 K showed four orders of magnitude reduction in dark current density (from $\sim 8 \times 10^{-3}$ to $\sim 5 \times 10^{-7} \text{ A/cm}^2$) at an applied bias

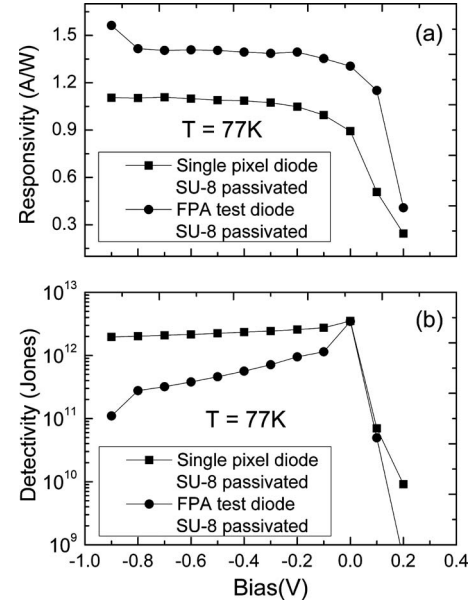


FIG. 5. (a) Responsivity and (b) Detectivity of SU-8 passivated single pixel and test FPA diode (at 77 K).

($V_b = -0.3 \text{ V}$), and fivefold increase in the surface (from $\sim 1.9 \times 10^2$ to $\sim 1.0 \times 10^3 \Omega \text{ cm}$) at 87 K. The FPA test pixel passivated with SU-8 at 77 K showed a reduction in dark current density by three orders of magnitude compared to a nonpassivated diode (from 8×10^{-3} to $3.4 \times 10^{-6} \text{ A/cm}^2$) at $V_b = -0.3 \text{ V}$. At 77 K, the zero bias responsivity and detectivity are equal to 0.9 A/W and 3.5×10^{12} Jones for a SU-passivated single diode, 1.3 A/W and 3.45×10^{12} Jones for the SU-passivated FPA test diode. These improved performances prove that SU-8 is a good passivation material for InAs/GaSb SLS FPAs. We intend to extend this work to long wavelength IR detectors in the future.

The authors would like to acknowledge the support by AFOSR under Grant No. FA9550-09-1-0231, AFRL under Grant No. FA9453-07-C-017, and KRISS-GRL program.

- ¹A. Rogalski, *Opto-Electron. Rev.* **16**, 458 (2008).
- ²D. L. Smith and C. Mailhot, *J. Appl. Phys.* **62**, 2545 (1987).
- ³E. Plis, J. B. Rodriguez, S. J. Lee, and S. Krishna, *Electron. Lett.* **42**, 1248 (2006).
- ⁴F. Fuchs, U. Weimer, W. Pletschen, J. Schmitz, E. Ahlswede, M. Walther, J. Wagner, and P. Koidl, *Appl. Phys. Lett.* **71**, 3251 (1997).
- ⁵E. K. Huang, D. Hoffman, B.-M. Nguyen, P.-Y. Delaunay, and M. Razeghi, *Appl. Phys. Lett.* **94**, 053506 (2009).
- ⁶A. Hood, P.-Y. Delaunay, D. Hoffman, B.-M. Nguen, Y. Wei, M. Razeghi, and V. Nathan, *Appl. Phys. Lett.* **90**, 233513 (2007).
- ⁷M. R. Ravi, A. DasGupta, and N. DasGupta, *J. Cryst. Growth* **268**, 359 (2004).
- ⁸E. H. Conradie and D. F. Moore, *J. Micromech. Microeng.* **12**, 368 (2002).
- ⁹T. A. Anhoj, A. M. Jorgensen, D. A. Zauner, and J. Hubner, *Proc. SPIE* **6110**, 611009 (2006).
- ¹⁰M. Shaw, D. Nawrocki, R. Hurditch, and D. Johnson, *Microsyst. Technol.* **10**, 1 (2003).
- ¹¹H. S. Kim, E. Plis, J. B. Rodriguez, G. D. Bishop, Y. D. Sharma, L. R. Dawson, S. Krishna, J. Bundas, R. Cook, D. Burrows, R. Dennis, K. Patnaude, A. Reisinger, and M. Sundaram, *Appl. Phys. Lett.* **92**, 183502 (2008).
- ¹²E. Plis, H. S. Kim, G. Bishop, S. Krishna, K. Banerjee, and S. Ghosh, *Appl. Phys. Lett.* **93**, 123507 (2008).

The effect of absorber doping on electrical and optical properties of nBn based type-II InAs/GaSb strained layer superlattice infrared detectors

Stephen Myers,¹ Elena Plis,¹ Arezou Khoshakhlagh,¹ Ha Sul Kim,¹ Yagya Sharma,¹ Ralph Dawson,¹ Sanjay Krishna,^{1,a)} and Aaron Gin²

¹Department of Electrical and Computer Engineering, Center for High Technology Materials, University of New Mexico, Albuquerque, New Mexico 87106, USA

²Center for Integrated Nanotechnologies, Sandia National Laboratories, P.O. Box 5800, Albuquerque, New Mexico 87185-1303, USA

(Received 17 July 2009; accepted 21 August 2009; published online 24 September 2009)

We have investigated the electrical and optical properties of a nBn based InAs/GaSb strained layer superlattice detector as a function of absorber region background carrier concentration. Temperature dependent dark current, responsivity, and detectivity were measured. The device with a nonintentionally doped absorption region demonstrated the lowest dark current density with a specific detectivity at zero bias equal to 1.2×10^{11} cm Hz^{1/2}/W at 77 K. This value decreased to 6×10^{10} cm Hz^{1/2}/W at 150 K. This contrasts significantly with *p-i-n* diodes, in which the D^* decreases by over two orders of magnitude from 77 to 150 K, making nBn devices promising for higher operating temperatures. © 2009 American Institute of Physics. [doi:10.1063/1.3230069]

Infrared (IR) detectors have a broad range of applications in civilian, medical, industrial, astronomical, and military fields. The technologies currently dominating the IR detector market (3–12 μm) are mercury cadmium telluride (MCT), indium antimonide (InSb), and quantum well infrared photodetectors (QWIP). However, lack of spatial uniformity over a large area and low yield for large focal plane arrays (FPAs) still plague MCT¹ devices. While InSb detectors dominate the mid wave infrared (MWIR, 3–5 μm) regime, their wavelength response is not tailorable due to a fixed bandgap and the devices are limited to cryogenic temperatures.² The QWIPs are based on a mature GaAs technology and demonstrate very good uniformity and reproducibility. However they have large dark currents and low quantum efficiencies compared to interband devices. The type-II strained layer superlattice (SLS) material system was first theoretically proposed by Tsu *et al.*³ in 1977. A decade later Smith and Mailhot⁴ demonstrated that the optical absorption for the InAs/(In,Ga)Sb SLS material is as good as the MCT alloy with the same bandgap. Since then the SLS material has generated significant interest in IR detection.

The InAs/GaSb SLS is characterized by a so called “broken-gap” type-II alignment, with the conduction band edge of InAs located lower than the valence band edge of GaSb. Spatially indirect optical transitions between holes localized in GaSb layers and electrons confined in InAs layers are employed for the detection of infrared radiation. By varying the composition and thickness of constituent layers, the effective bandgap of an InAs/GaSb detector can be tuned between 3 and 30 μm. The SLS is characterized by reduced Auger recombination rates due to the spatial separation of electrons and holes.⁵ In contrast with QWIPs,⁶ normal incidence absorption is permitted in SLS resulting in high quantum efficiency. In addition, the electron effective mass is not dependent on the bandgap size and is larger than that measured in MCT detectors⁷ which leads to reduced tunneling

currents. Commercial availability of low defect density substrates and a high degree of uniformity for III-V processing over a large area also offers technological advantages for the SLS. This makes detectors based on SLs an attractive technology for realization of high performance single element detectors and FPAs.^{8–13}

Presently most SLS detectors are based on a photodiode (*p-on-n* or *n-on-p*) design. In this case, two main contributions to dark current are surface leakage currents associated with the mesa sidewall exposure, which defines the device optical area, and generation-recombination current associated with Shockley–Read–Hall (SRH) centers in the depletion region of the photodiode. With scaling of device dimensions (typical dimensions of an FPA pixel is $\sim 20 \times 20$ μm²), the surface/volume ratio is increased and detector performance is strongly dependent on surface effects. In order to overcome the limitation imposed by surface leakage currents, a stable surface passivation layer is needed. Various research groups have developed different passivation and coating processes that are stable, insensitive to the device cutoff wavelength and easily integrated into fabrication processes.^{14–17}

The nBn detector structure was recently proposed¹⁸ which utilizes both a wide-bandgap barrier to block majority carriers and a buried, planar device structure effectively eliminating surface currents. In addition, it excludes the SRH generation-recombination component of dark current since it is intended to operate with *n*-type layers in flatband or with little depletion. The typical SLS photodetector with an nBn design is formed by a nonintentionally doped (NID) thick SLS absorber layer grown on the top of a *n*-type bottom contact layer, followed by a 100 nm barrier layer and capped by a thin *n*-type contact layer.^{19,20} Due to a nearly zero valence band offset and a large conduction band offset, the majority carrier current between the two electrodes is blocked, while photogenerated minority carriers do not see a barrier. Due to processing utilized for nBn detectors, the size of the device, unlike a conventional photodiode, is not defined by the dimensions of the etched mesa but by the lateral

^{a)}Author to whom correspondence should be addressed. Electronic mail: skrishna@chtm.unm.edu.

diffusion length of minority carriers (holes). The second recently proposed approach for realization of room temperature detectors utilizes heavy hole/light hole to split-off transitions. With this design a D^* of 6.8×10^5 Jones at $2.5 \mu\text{m}$ operating at 300 K has been achieved.²¹

It is well known that for the design of narrow bandgap photodiodes the doping level in the absorber regions is a very important parameter that affects the electrical and optical performance of the device.²² However, the effect of the absorber doping on nBn devices has not been studied before. In this paper, we have investigated the electrical and optical properties of an nBn based InAs/GaSb SLS MWIR detector as a function of background carrier concentration of the absorber. Temperature-dependent dark current, responsivity, and detectivity of the nBn MWIR detector as a function of absorber doping were measured.

The detector structures were grown on *n*-type (Te-doped) GaSb (100) epitaxial substrates using solid source molecular beam epitaxy in a VG-80 system equipped with valved cracker sources for group V Sb_2 and As_2 fluxes and Ga/In SUMO[®] cells. Growth details have been reported elsewhere.²³ The device structure consists of a $\sim 1 \mu\text{m}$ 10 monolayers (MLs) InAs/10 MLs GaSb SLS (170 periods) absorber grown on top of a $\sim 0.36 \mu\text{m}$ thick *n*-type contact layer (composed of the SLS with the same composition and thickness but with Si-doped InAs layers). This was followed by a 100 nm $\text{Al}_{0.2}\text{Ga}_{0.8}\text{Sb}$ NID (*p*-type) barrier layer and a 20 nm GaSb NID spacer layer. The structure was capped by a $\sim 0.1 \mu\text{m}$ thick top contact layer with the same superlattice composition, thickness, and doping concentration as the bottom contact layer. The doping concentration of the absorbing region was equal to $5 \times 10^{16} \text{ cm}^{-3}$ (NID SLS material), $1.4 \times 10^{17} \text{ cm}^{-3}$, $4.0 \times 10^{17} \text{ cm}^{-3}$, and $3.5 \times 10^{18} \text{ cm}^{-3}$ as determined from Hall measurements on samples grown on GaAs substrates. The material was processed into normal incidence single-pixel detectors with $410 \mu\text{m} \times 410 \mu\text{m}$ mesas with apertures varying from 25 to $300 \mu\text{m}$ in diameter using standard optical photolithography and dry etching techniques.

The spectral response of the detectors was measured with a Nicolet 670 Fourier transform infrared spectrometer relative to a standard deuterated triglycine sulfate thermal detector. The 100%-cut-off wavelength of the NID detector is equal $\sim 6 \mu\text{m}$ whereas the detector with the largest doping level ($n = 3.5 \times 10^{18} \text{ cm}^{-3}$) shows a 100% cutoff wavelength at $\sim 4.5 \mu\text{m}$. The observed blueshift of cutoff wavelength is attributed to the Moss–Burstein effect. Absolute comparison of the response of the four detectors measured at $T = 77 \text{ K}$ with a bias of $V_b = 0.1 \text{ V}$ is presented in Fig. 1.

Current-voltage (*IV*) characteristics were measured for the devices at 77 K using a HP4145 semiconductor parameter analyzer as shown in Fig. 2. It should be noted that the forward bias is defined as a positive voltage applied to the bottom contact of the device. At 77 K and 0.1 V of applied bias, the dark current density increases by three orders of magnitude (from $\sim 0.3 \text{ mA/cm}^2$ to $\sim 0.3 \text{ A/cm}^2$), when the doping concentration is changed from 5×10^{16} to $3.5 \times 10^{18} \text{ cm}^{-3}$. The observed increase in dark current density of the nBn detector with increased doping of the absorption region contradicts our expectations. Since the nBn detector is designed to operate as a minority (hole) carrier photoconductor device in flatband conditions, the *n*-type doping level of

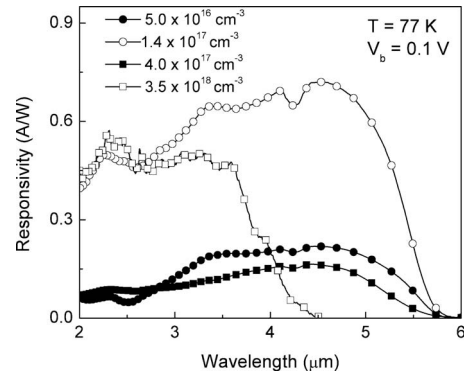


FIG. 1. Responsivity of the four detectors with doping concentrations of 5.0×10^{16} (NID), 1.4×10^{17} , 4.0×10^{17} , and $3.5 \times 10^{18} \text{ cm}^{-3}$ at $T = 77 \text{ K}$ with a bias of $V_b = 0.1 \text{ V}$.

the absorbing region is not supposed to influence device operation.²⁴ For a conventional photodiode, the increase of absorber doping above 10^{16} cm^{-3} would result in a very thin depletion region and Zener breakdown,²⁴ which is not the case for the unipolar nBn detector device. We believe that this increase in the dark current suggests that there is a quantum well (QW) for the minority carriers (holes) formed in the valence band. With an increase in the doping level of the absorber the depth of this QW increases. We think, during the device operation holes may be trapped in the QW whereas electrons are accumulated near the barrier. This leads to an enhanced electron-hole recombination. Thus, for the higher doped absorber region the carrier lifetime will be decreased due to the increase in electron-hole recombination. Since dark current is inversely proportional to the carrier lifetime, the increase in dark current density is expected and observed for the higher doped devices.

Specific detectivity (D^*) was estimated using the following equation:

$$D^* = R_\lambda / \sqrt{2qJ + (4kT)/(R_d A_d)}, \quad (1)$$

where R_λ is the responsivity, q is the electronic charge, J is the dark current density, k is the Boltzmann constant, T is the temperature of the device, R_d is the dynamic resistance, and A_d is the diode area. The D^* was calculated at $4.4 \mu\text{m}$ for all studied detectors.

The responsivity was measured using a Stanford Research SR770 FFT network analyzer and a Mikron blackbody set to 800°C . At 150 K, responsivity reached 1 A/W at zero bias.

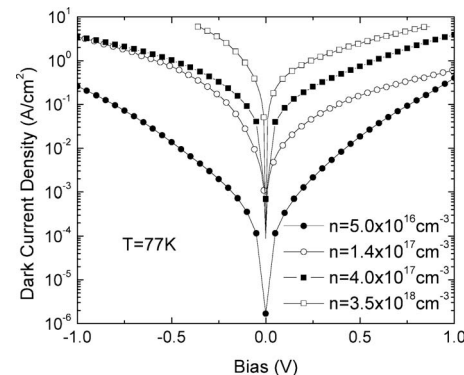


FIG. 2. Dark current density vs applied bias of the detectors with four different doping concentrations at 77 K.

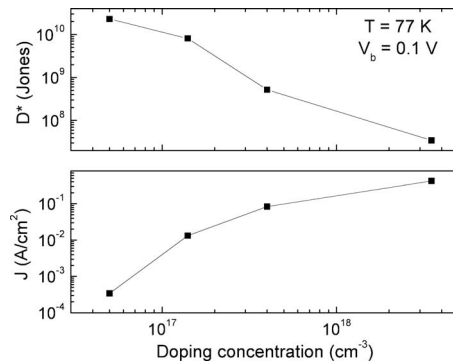


FIG. 3. Specific detectivity and dark current density as a function of doping concentration in absorption region of nBn MWIR detector ($V_b=0.1$ V and $T=77$ K).

The low-temperature (77 K) dependencies of specific detectivity along with the dark current density as a function of n -type doping level of the absorption region are presented in Fig. 3 ($V_b=0.1$ V). The significant degradation of both parameters with increased n -type doping level of the absorbing region is observed. The maximum detectivity that was measured was 2.3×10^{10} Jones for the NID device (0.1 V). The bias-dependent values of D^* at 77 K for the four devices are shown in Fig. 4.

The temperature dependence of D^* for the NID detector was also investigated. The zero bias D^* was estimated to be 6×10^{10} Jones at 150 K for the NID device, which is comparable with state-of-the-art p - i - n diodes at the same operating temperature.²⁵ At 0.1 V of applied bias, D^* was found to be $\sim 1.6 \times 10^{10}$ Jones. Thus, no significant degradation of D^* within (0–100) mV bias range with temperature was observed and the corresponding change in dark current density was less than an order of magnitude. For the p - i - n photodiode with nearly the same cut-off wavelength the D^* decreases by more than two orders of magnitude from 77 to 150 K²⁵ for the same bias range.

In conclusion, we have investigated the electrical and optical properties of a MWIR nBn detector as a function of background carrier concentration in the absorbing region of the device. Contrary to our expectations, dark current density was dramatically affected by the change of the n -type doping level in the detector absorption region. Such behavior can be

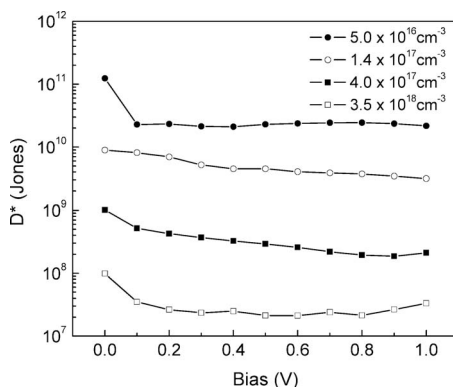


FIG. 4. Bias-dependent specific detectivity of the four detectors with doping concentrations of 5.0×10^{16} (NID), 1.4×10^{17} , 4.0×10^{17} , and 3.5×10^{18} cm^{-3} measured at $T=77$ K.

attributed to the presence of a QW for the minority carriers (holes) formed in the valence band. The device with the NID doping level in the absorption region demonstrated the best performance among all studied samples with zero-bias values of current responsivity and specific detectivity equal to 1 A/W and 6.0×10^{10} Jones, respectively, (150 K) with a 0% cutoff near 6 μm . The observed temperature dependence of D^* is significantly different from conventional p - i - n diodes, in which the D^* decreases by over two orders of magnitude from 77 to 150 K, making nBn devices a promising alternative for achieving higher operating temperatures.

The authors would like to acknowledge support from AFRL Contract No. FA9453-07-C-0171 and AFOSR Contract No. FA9550-09-1-0231. This work was performed, in part, at the Center for Integrated Nanotechnologies, a U.S. Department of Energy, Office of Basic Energy Sciences user facility. Sandia National Laboratories is a multiprogram laboratory operated by Sandia Corporation, a Lockheed-Martin Co., for the U.S. Department of Energy under Contract No. DE-AC04-94AL85000.

- ¹P. Norton, *Opto-Electron. Rev.* **10**, 159 (2002).
- ²W. J. Parrish, J. D. Blackwell, R. C. Paulson, and H. Arnold, *Proc. SPIE* **1512**, 68 (1991).
- ³G. A. Sai-Halasz, R. Tsu, and L. Esaki, *Appl. Phys. Lett.* **30**, 651 (1977).
- ⁴D. L. Smith and C. Mailhot, *J. Appl. Phys.* **62**, 2545 (1987).
- ⁵H. Mohseni, V. Litvinov, and M. Razeghi, *Phys. Rev. B* **58**, 15378 (1998).
- ⁶B. F. Levine, *J. Appl. Phys.* **74**, R1 (1993).
- ⁷A. Rogalski, *Opto-Electron. Rev.* **14**, 84 (2006).
- ⁸E. Plis, J. B. Rodriguez, H. S. Kim, G. Bishop, Y. D. Sharma, L. R. Dawson, S. Krishna, S. J. Lee, C. E. Jones, and V. Gopal, *Appl. Phys. Lett.* **91**, 133512 (2007).
- ⁹M. Razeghi, D. Hoffman, B.-M. Nguyen, P.-Y. Delaunay, E. K.-W. Huang, and M. Z. Tidrow, *Proc. SPIE* **6940**, 694009 (2008).
- ¹⁰M. Walther, R. Rehm, J. Schmitz, F. Rutz, J. Fleissner, and J. Ziegler, *Proc. SPIE* **6940**, 69400A (2008).
- ¹¹B.-M. Nguyen, D. Hoffman, Y. Wei, P.-Y. Delaunay, A. Hood, and M. Razeghi, *Appl. Phys. Lett.* **90**, 231108 (2007).
- ¹²J. Li, C. Hill, J. Mumolo, S. Gunapala, S. Mou, and S. Chuang, *Appl. Phys. Lett.* **93**, 163505 (2008).
- ¹³I. Vurgaftman, E. Aifer, C. Canedy, J. Tischler, J. Meyer, J. Warner, E. Jackson, G. Hildebrandt, and G. Sullivan, *Appl. Phys. Lett.* **89**, 121114 (2006).
- ¹⁴A. Gin, Y. Wei, A. Hood, A. Bajowala, V. Yazdanpanah, and M. Razeghi, *Appl. Phys. Lett.* **84**, 2037 (2004).
- ¹⁵A. Hood, P.-Y. Delaunay, D. Hoffman, B.-M. Nguyen, Y. Wei, and M. Razeghi, *Appl. Phys. Lett.* **90**, 233513 (2007).
- ¹⁶E. Plis, J. B. Rodriguez, S. J. Lee, and S. Krishna, *Electron. Lett.* **42**, 1248 (2006).
- ¹⁷R. Rehm, M. Walther, F. Fuchs, J. Schmitz, and J. Fleissner, *Appl. Phys. Lett.* **86**, 173501 (2005).
- ¹⁸S. Maimon and G. W. Wicks, *Appl. Phys. Lett.* **89**, 151109 (2006).
- ¹⁹J. Rodriguez, E. Plis, G. Bishop, Y. D. Sharma, H. Kim, L. R. Dawson, and S. Krishna, *Appl. Phys. Lett.* **91**, 043514 (2007).
- ²⁰G. Bishop, E. Plis, J. B. Rodriguez, Y. D. Sharma, H. S. Kim, L. R. Dawson, and S. Krishna, *J. Vac. Sci. Technol. B* **26**, 1145 (2008).
- ²¹P. V. Jayaweera, S. G. Matsik, A. G. U. Perera, H. C. Liu, M. Buchanan, and Z. R. Wasilewski, *Appl. Phys. Lett.* **93**, 021105 (2008).
- ²²D. Hoffman, B.-M. Nguyen, P.-Y. Delaunay, A. Hood, M. Razeghi, and J. Pellegrino, *Appl. Phys. Lett.* **91**, 143507 (2007).
- ²³E. Plis, S. Annamalai, K. T. Posani, S. Krishna, R. A. Rupani, and S. Ghosh, *J. Appl. Phys.* **100**, 014510 (2006).
- ²⁴P. Klipstein, *Proc. SPIE* **6940**, 69402U (2008).
- ²⁵Y. Wei, A. Hood, H. Yau, M. Razeghi, M. Z. Tidrow, and V. Nathan, *Appl. Phys. Lett.* **86**, 233106 (2005).

Accepted Manuscript

Heterojunction Bandgap Engineered Photodetector Based on Type-II InAs/GaSb Superlattice for Single Color and Bicolor Infrared Detection

N. Gautam, H.S. Kim, S. Myers, E. Plis, M.N. Kutty, Mikhail Naydenkov, B. Klein, L.R. Dawson, S. Krishna

PII: S1350-4495(10)00129-5

DOI: [10.1016/j.infrared.2010.12.028](https://doi.org/10.1016/j.infrared.2010.12.028)

Reference: INFPHY 1133

To appear in: *Infrared Physics & Technology*



Please cite this article as: N. Gautam, H.S. Kim, S. Myers, E. Plis, M.N. Kutty, M. Naydenkov, B. Klein, L.R. Dawson, S. Krishna, Heterojunction Bandgap Engineered Photodetector Based on Type-II InAs/GaSb Superlattice for Single Color and Bicolor Infrared Detection, *Infrared Physics & Technology* (2010), doi: [10.1016/j.infrared.2010.12.028](https://doi.org/10.1016/j.infrared.2010.12.028)

This is a PDF file of an unedited manuscript that has been accepted for publication. As a service to our customers we are providing this early version of the manuscript. The manuscript will undergo copyediting, typesetting, and review of the resulting proof before it is published in its final form. Please note that during the production process errors may be discovered which could affect the content, and all legal disclaimers that apply to the journal pertain.

Heterojunction Bandgap Engineered Photodetector Based on Type-II InAs/GaSb Superlattice for Single Color and Bicolor Infrared Detection

N. Gautam*, H.S. Kim, S. Myers, E. Plis, M. N. Kutty, Mikhail Naydenkov, B. Klein,

L. R. Dawson and S. Krishna

Center for High Technology Materials, Department of Electrical and Computer Engineering,
University of New Mexico, Albuquerque, NM 87106

* Corresponding author: 1313 Goddard St SE, Albuquerque, NM, 87106.

Tel: + 1 818 505 272 7849; Fax: + 1 818 505 272 7801. E-mail address: nutan@chtm.unm.edu

Keywords: Infrared detectors, strained layer superlattice, longwave infrared, unipolar barriers, dual color.

We report a heterostructure bandgap engineered strained layer superlattice photodetector design for performance improvement for longwave infrared (LWIR) detection. At 77K, the dark current density of the reported device was at least two orders of magnitude lower than that of the conventional PIN superlattice photodiode. We have obtained a shot-noise limited detectivity of $8.7 \times 10^{10} \text{ cm-Hz}^{1/2} \text{ W}^{-1}$ ($\lambda_c = 10.8 \text{ }\mu\text{m}$), responsivity of 1.8A/W, 23% QE at 250mV of applied reverse bias. A three contact heterojunction bandgap engineered dual color detector was demonstrated with simultaneous detection of midwave and longwave infrared radiation. The design showed midwave responsivity of 0.93A/W and detectivity of $1.0 \times 10^{11} \text{ cm-Hz}^{1/2} \text{ W}^{-1}$ (at 4 μm) at 77K for $V_b = -70\text{mV}$. Longwave responsivity and detectivity of 1.5 A/W and $2.42 \times 10^{10} \text{ cm-Hz}^{1/2} \text{ W}^{-1}$ (at 10 μm) were observed at -100mV of applied bias at 77K.

1. Introduction

Type-II InAs/GaSb strained layer superlattices (SLS) [1,2] have become very important for infrared applications. Detectors based on type-II SLS have demonstrated promising performance in midwave infrared (MWIR) and longwave infrared (LWIR) regimes. Although the current performance of SLS is not yet near the theoretical predictions, it has several advantages over existing technologies in infrared detection. Auger recombination is significantly suppressed in SLS as compared to HgCdTe (MCT) detectors [3] and also growth and fabrication is easier because of III-V based material system. SLS material system suffers from disadvantages of surface leakage current and high Shockley-Read-Hall (SRH) currents. While a good surface passivation is still a technological challenge, efforts have been made to reduce SRH current by barrier engineering of SLS devices.

One of the key features of SLS system is the freedom of bandgap and band offset tunability by changing the thickness of InAs and GaSb layers, which has resulted in a number of heterostructure designs present in the literature. Some of the designs are M-structure [4], nBn [5], W-structure [6] and complementary barrier infrared detector (CBIRD) [7]. These heterostructure designs have shown significant improvement over conventional homojunction PIN photodiode. We recently proposed heterojunction architecture known PbIbN [8], which is a modification of PIN photodiode with an electron barrier (EB) between P contact layer and absorber region and a hole barrier (HB) between absorber region and N contact layer. The EB layer sandwiched between P contact layer and absorber region blocks the minority carrier diffusion (electrons) current from P contact layer into the absorber region. Similarly the HB layer blocks minority carrier diffusion (holes) current from N contact layer into the absorber region. Moreover, the electric field drop across the active region is small as compared to a conventional

PIN design since there is significant amount of field drop across the EB and HB layers, which have wider bandgap compared to the absorber region. This reduction in electric field leads to small depletion region and hence reduction in the SRH current. Further tunneling currents are also reduced due to significant reduction in field drop.

We report here performance improvement of PbIbN device over PIN diode. The PbIbN design has shown over two orders of magnitude reduction in dark current, over a conventional PIN design, at an applied reverse bias of 250mV, with dark current shot noise limited detectivity of $8.7 \times 10^{10} \text{ cm-Hz}^{1/2} \text{ W}^{-1}$ and responsivity of 1.8 A/W with a 10.8 μm cut-off wavelength at 77K.

We also report a novel heterojunction design for dual color infrared detector which consists of MWIR and LWIR absorbing regions. This type of device structure is very important for applications which require simultaneous detection of MWIR and LWIR infrared signals. The device structure consists of a PbIbN LW detector design and PbIN design for MW detection. The PbIN design has barrier only for electrons and not for holes. LW and MW detection regions share common N contact and hence it is a three contact device. This device design has shown responsivity of 0.93 A/W and 1.5A/W and detectivity of $1.0 \times 10^{11} \text{ cm-Hz}^{1/2} \text{ W}^{-1}$ and $2.42 \times 10^{10} \text{ cm-Hz}^{1/2} \text{ W}^{-1}$ for MW and LW respectively at 77K. The LWIR and MWIR detection regions have 50% cut-off wavelength (λ_c) of 10.6 μm and 5.5 μm respectively.

2. Growth and Processing

Detector structures were grown on Te doped epi-ready (100) GaSb substrate using a solid source molecular beam epitaxy VG80 system. The system was equipped with SUMO ® cells for gallium and indium and cracker cells for antimony and arsenic. Growth rates were calibrated by monitoring the intensity oscillations in the reflected high-energy electron diffraction (RHEED)

patterns and confirmed with X-Ray diffraction by growth of calibration superlattice samples with different thicknesses of SLS periods. The heterostructure schematic of PbIbN design along with band diagram has been shown in Fig. 1 (a), where notation $N(\text{InAs}) \text{ ML} / M(\text{GaSb}) \text{ ML}$ is used. The PbIbN design has 637 nm thick N contact layer made of 16ML InAs/ 7ML GaSb doped with Te ($n=3\times 10^{18} \text{ cm}^{-3}$) followed by non-intentionally doped (n.i.d) 450 nm thick HB layer made of 13ML InAs/ 4ML GaSb SLS. This is followed by a 2.2 μm thick n.i.d absorber region of 14ML InAs/ 7ML GaSb SLS and an EB layer of n.i.d 325 nm thick 8ML InAs/ 8ML GaSb SLS. A 138 nm thick 13ML InAs/ 8ML GaSb SLS P contact layer doped with Be ($p=2.8\times 10^{18} \text{ cm}^{-3}$) completes the structure. The PIN device, used for comparison, has 609 nm thick Te doped N contact layer ($n = 3\times 10^{18} \text{ cm}^{-3}$) consisting of 14ML InAs/ 7ML GaSb SLS followed by a 159 nm thick graded n-doping region. This is followed by 2.1 μm thick n.i.d absorber region of 14ML InAs/ 7ML GaSb SLS, followed by p-type graded doping region, 159 nm thick, of 14/7 SLS. The topmost layer is 100nm thick Be doped GaSb P contact layer ($p = 2.8\times 10^{18} \text{ cm}^{-3}$).

The dual color detector schematic and band diagram is shown in Fig. 1(b). The MW detection region is stacked on top of LW region, which can be called as a PbIN design while the LW detection region is PbIbN design which shares common N contact with the MW region. This is a top side illumination device. This device design consists of bottom P+ contact layer ($p = 2.8\times 10^{18} \text{ cm}^{-3}$) made of 94 periods of 13ML InAs/8ML GaSb. It was then followed by 30 periods of EB layer (n.i.d.) made of 8ML InAs/8ML GaSb SLS, on top of which 282 Periods of n.i.d 14ML InAs/ 7ML GaSb SLS LW absorber region was grown. Then n.i.d HB layer consisting of 48 periods of 13ML InAs/4ML GaSb SLS, which was followed by N+ contact layer ($n= 3\times 10^{18} \text{ cm}^{-3}$) made of 72 periods of 16ML InAs/ 7ML GaSb SLS and acts as the common contact layer for MW and LW detection regions. On top of middle contact layer, 280 periods of MW absorber

region, made of 10ML InAs/10ML GaSb SLS, was grown. It then followed growth of 100nm thick $\text{Al}_{0.2}\text{Ga}_{0.8}\text{Sb}$ EB layer for MW SLS and on top of it P+ contact layer ($p=2.8\times 10^{18} \text{ cm}^{-3}$) made of 50nm thick GaSb completed the structure.

After the MBE growth, the material was processed into single pixel device arrays using inductively coupled plasma (ICP) dry etching. Optical apertures to the device were then defined by photolithography for contact metal deposition, with aperture diameter ranging from $25\mu\text{m}$ to $300\mu\text{m}$. An ohmic contact was made by depositing Ti/Pt/Au on the bottom and top contact layers of the detectors. The devices were then passivated with SU-8 [9], an epoxy-based negative photoresist, to reduce surface leakage current.

3. Results and Discussion

After device processing, radiometric characterization and dark current measurements were carried out. Fig. 2(a) shows normalized spectral response (SR) for PbIbN and PIN devices at 77K at -0.2V of applied bias, with λ_c of $10.8 \mu\text{m}$ and $11 \mu\text{m}$ respectively. Spectral response for longwave devices has been shown for wavelengths higher than or equal to $8.4 \mu\text{m}$ because all the radiometric measurements reported in this paper have been undertaken using a longwave bandpass filter ($8.4 - 11.5 \mu\text{m}$).

Fig. 2(b) compares dark currents of PbIbN design with PIN design at various temperatures. At 77K, PbIbN design has reduced dark current by a factor of 140 over PIN ($V_b = -0.25\text{V}$). This decrease in dark current is attributed to the barriers incorporated in the PbIbN design. The EB layer sandwiched between P contact layer and absorber region blocks diffusion of minority carrier electrons from P contact into the absorber region, similarly HB blocks minority carrier holes from N contact layer to absorber region hence reducing the dark current. The performance

improvement of PbIbN over PIN design can be explained using Fig. 3(a), which shows the electric field profile at -250mV of applied bias. For calculation of electric field, the EB layer has been approximated to have $1 \times 10^{16} \text{ cm}^{-3}$ p-type doping while absorber region and HB layers with $8 \times 10^{15} \text{ cm}^{-3}$ and $1 \times 10^{16} \text{ cm}^{-3}$ n-type doping respectively [10]. The electric field drop across the active region is small in PbIbN design as compared to PIN design since there is significant amount of field drop across the EB and HB layers, which have a wider bandgap compared to the absorber region. This reduction in electric field leads to very small depletion region and hence reduction in the SRH current. Further tunneling currents are also reduced due to significant reduction in field drop. Since, the device design prefer majority of electric field drop across the wider bandgap barrier regions and hence reducing the SRH currents as well as tunneling currents. Fig. 3(b) shows Arrhenius plot of dark current density against temperature for PIN and PbIbN designs. This plot has been used to calculate activation energies, which gives an insight about the dark current mechanisms in PIN and PbIbN devices. It shows that till 175K dark current of PIN device is dominated by G-R currents, as the activation energy for this temperature range is close to $E_g/2$, where E_g refers to bandgap, while at higher temperatures, the diode becomes very leaky and resistance of the device becomes comparable to the contact resistance. Hence a very low value of activation energy is observed at higher temperatures. For PbIbN device, we still see SRH current dominance of dark current till 150K, as revealed by the activation energy being $\sim E_g/2$, but beyond 150K the dark current characteristic is dominated by diffusion dark current. The activation energy beyond 150K is close to bandgap energy (0.0902 eV), which is slight underestimation of bandgap energy.

The responsivity measurements were carried out at different temperatures using a calibrated black-body source at 900K. Fig. 4 shows measured responsivity of both PbIbN and PIN designs at $\lambda=10\ \mu\text{m}$ at 77K. It is to be noted that responsivity of PbIbN design is less than that of PIN and this decrease is due to the fact that the EB and HB layers impede the flow photogenerated holes and electrons respectively. Since, this was the first structure for the proof of concept, there is a huge scope of improvement in barrier and doping optimization in this structure. Photoconductive gain was assumed to be unity for calculating QE. It is to be noted that no anti-reflection coating (ARC) is used in these devices. The responsivity value at -0.25 V is 1.8 A/W with 23% QE for PbIbN while for PIN it is 3.8 A/W at -0.1V. The shot noise limited D^* was calculated, from dark current, at $10\ \mu\text{m}$ using the following equation.

$$D^* = \frac{R}{\sqrt{2qJ_d + (4kT)/R_d A_d}} \quad (1)$$

Where R is the responsivity, q is the electronic charge, T is the temperature of the device, k is Boltzmann's constant, J_d is the dark current density, R_d is the dynamic resistance, and A_d is the diode area. Fig. 4 shows calculated D^* for PbIbN and PIN device at 77K at $10\ \mu\text{m}$ wavelength. At 77K, a peak D^* of $8.7 \times 10^{10}\ \text{cm Hz}^{1/2}\ \text{W}^{-1}$ is observed at -0.25 V, while PIN design has a peak detectivity of $2.2 \times 10^{10}\ \text{cm Hz}^{1/2}\ \text{W}^{-1}$ at -0.1V of applied bias, which indicates that the PbIbN design improves detectivity by a factor of four over PIN design. Measurements were also carried out at higher temperature, at 85K and 95K, the peak D^* is $5 \times 10^{10}\ \text{cm Hz}^{1/2}\ \text{W}^{-1}$ and $2.1 \times 10^{10}\ \text{cm Hz}^{1/2}\ \text{W}^{-1}$ at -0.4 V and -0.5V respectively for the PbIbN design. The RA product of PbIbN at peak detectivity bias ($V_b=-0.25\text{V}$) was found to be $74\ \Omega\text{-cm}^2$ while for PIN at peak detectivity bias ($V_b=-0.1\text{V}$) it was $2\ \Omega\text{-cm}^2$.

The dual color detector was characterized in a similar way as the single color PbIbN device. The device design allows biasing to both midwave and longwave region simultaneously. Normalized spectral response has been shown for both midwave and longwave devices at 77K under 0V of applied bias in Fig. 5(a) and 5(b) respectively. Fig. 6 shows current voltage characteristic of the device for MW as well as LW region at 80K. The unipolar barriers enhance the performance of the device in similar fashion as has been mentioned earlier for the single color device. Dual color detectors have been reported earlier in the literature [11, 12, 13]. The advantage of this design over earlier mentioned structure is that the dark current can be reduced significantly for the longwave device and simultaneous and independent detection of longwave and midwave signals can be carried out.

Fig. 7 shows responsivity and detectivity, as a function of bias, for midwave and longwave detectors at 77K at 4 μm and 10 μm respectively. Shot-noise limited detectivity was calculated using equation (1). As can be seen from Fig. 7 peak detectivity for MW and LW regimes is $1.0 \times 10^{11} \text{ cm-Hz}^{1/2} \text{ W}^{-1}$ (at 4 μm) and $2.42 \times 10^{10} \text{ cm-Hz}^{1/2} \text{ W}^{-1}$ (at 10 μm) at -70mV and -0.1V of applied bias where responsivity is 0.93A/W and 1.5A/W respectively.

4. Conclusions

In conclusion we have reported a heterojunction detector design, PbIbN, consisting of unipolar barriers to improve the performance of longwave infrared detectors made of InAs/GaSb strained layer superlattice system. PbIbN detector, at 77K, has shown almost two orders of magnitude improvement in dark current density over PIN with $\lambda_c=10.8 \mu\text{m}$, responsivity and detectivity of 1.8A/W and $8.7 \times 10^{10} \text{ cm Hz}^{1/2} \text{ W}^{-1}$ at -0.25 V ($\lambda=10.0 \mu\text{m}$). Also, the PbIbN detector design was extended to design a dual color (MW and LW) detector structure which incorporated PbIbN

design for LW and PbIN design for MW. At 77K, detectivity of $1.0 \times 10^{11} \text{ cm-Hz}^{1/2} \text{ W}^{-1}$ (at 4 μm) and $2.42 \times 10^{10} \text{ cm-Hz}^{1/2} \text{ W}^{-1}$ (at 10 μm) was observed for MW and LW signals at 70mV and 100mV of applied reverse biases respectively.

Work supported by AFOSR FA 9550-09-1-0231.

References:

- [1] G. A. Sai-Halasz, R. Tsu, and L. Esaki, A new semiconductor superlattice, *Appl. Phys. Lett.* 30 (1977) 651-653.
- [2] D. L. Smith and C. Mailhot, Proposal for strained type II superlattice infrared detectors, *J. Appl. Phys.* 62 (1987) 2545-2548.
- [3] C. H. Grein, M. E. Flatte, T. C. Hasenberg, J. T. Olesberg, S. A. Anson, L. Zhang, and T. F. Boggess, Auger recombination in narrow-gap semiconductor superlattices incorporating antimony, *J. Appl. Phys.* 92 (2002) 7311-7316.
- [4] B. M. Nguyen, D. Hoffman, P. Y. Delaunay, and M. Razeghi, Dark current suppression in type II InAs/GaSb superlattice long wavelength infrared photodiodes with M-structure barrier, *Appl. Phys. Lett.* 91 (2007) 163511-163513.
- [5] J. B. Rodriguez, E. Plis, G. Bishop, Y. D. Sharma, H. Kim, L. R. Dawson, and S. Krishna, nBn structure based on InAs/GaSb type-II strained layer superlattices, *Appl. Phys. Lett.* 91 (2007) 043514-043515.
- [6] I. Vurgaftman, E. H. Aifer, C. L. Canedy, J. G. Tischler, J. R. Meyer, J. H. Warner, E. M. Jackson, G. Hildebrandt, and G. J. Sullivan, Graded band gap for dark-current suppression in long-wave infrared W-structured type-II superlattice photodiodes, *Appl. Phys. Lett.* 89 (2006) 121114-121116.

- [7] David Z.-Y. Ting, Cory J. Hill, Alexander Soibel, Sam A. Keo, Jason M. Mumolo, Jean Nguyen, and Sarath D. Gunapala, A high-performance long wavelength superlattice complementary barrier infrared detector, *Appl. Phys. Lett.* 95 (2009) 023508-023510.
- [8] N. Gautam, H. S. Kim, M. N. Kuttly, E. Plis, L. R. Dawson, and S. Krishna, Performance improvement of longwave infrared photodetector based on type-II InAs/GaSb superlattices using unipolar current blocking layers, *Appl. Phys. Lett.* 96 (2010) 231107-231109.
- [9] H. S. Kim, E. Plis, N. Gautam, A. Khoshakhlagh, S. Myers, M. N. Kuttly, Y. Sharma, L. R. Dawson, and S. Krishna, SU-8 passivation of type-II InAs/GaSb strained layer superlattice detectors, *Proc. SPIE* 7660 (2010) 76601U-1- 76601U-9.
- [10] A. Khoshakhlagh, F. Jaeckel, C. Hains, J. B. Rodriguez, L. R. Dawson, K. Malloy, and S. Krishna, Background carrier concentration in midwave and longwave InAs/GaSb type II superlattices on GaAs substrate, *Appl. Phys. Lett.* 97 (2010) 051109-051111.
- [11] A. Khoshakhlagh, J. B. Rodriguez, E. Plis, G. D. Bishop, Y. D. Sharma, H. S. Kim, L. R. Dawson, and S. Krishna, Bias dependent dual band response from InAs/Ga(In)Sb type II strain layer superlattice detectors, *Appl. Phys. Lett.* 91 (2007) 263504-263506.
- [12] Pierre-Yves Delaunay, Binh-Minh Nguyen, Darin Hoffman¹, Andrew Hood¹, Edward Kwei-Wei Huang, Manijeh Razeghi, and Meimei Z. Tidrow, High quantum efficiency two color type-II InAs/GaSb n-i-p-p-i-n photodiodes, *Appl. Phys. Lett.* 92 (2008) 111112-111114.
- [13] R. Rehm, M. Walther, J. Fleißner, J. Schmitz, J. Ziegler, W. Cabanski, and R. Breiter, Bispectral thermal imaging with quantum-well infrared photodetectors and InAs/GaSb type-II superlattices, *Proc. SPIE* 6206 (2006) 62060Y-1-62060Y-11.

Figure captions:

Figure 1. Heterostructure Schematic of (a) PbIbN Design, (b) Dual Color Detector Design with flat band energy lineups.

Figure 2. (a) Spectral response of PbIbN and PIN designs at -0.2V of applied bias at 77K, (b) Dark current density of PbIbN and PIN designs versus applied bias at different temperatures.

Figure 3. (a) Calculated electric field profiles across PIN and PbIbN designs for 250mV of applied bias, (b) Arrhenius plot of $\ln(J)$ against temperature for PIN and PbIbN designs.

Figure 4. Responsivity and detectivity of PbIbN and PIN designs against bias at 77K.

Figure 5. Spectral response of dual color detector for (a) Midwave radiation, (b) Longwave radiation.

Figure 6. Dark current density of dual color detector across midwave and longwave detection regions at 80K.

Figure 7: Responsivity and Detectivity of Dual Color detector at 77K, for MW as well as LW radiation.

Figure 1(a)

138nm 13ML/8ML (a) ($p = 2.8 \times 10^{18} \text{ cm}^{-3}$)
325nm EB 8ML/8ML (n.i.d.)
2.2μm 14ML/7ML SLS (n.i.d.)
450nm HB 13ML/4ML SLS (n.i.d.)
637nm 16ML/7ML SLS ($n=3 \times 10^{18} \text{ cm}^{-3}$)
GaSb:Te

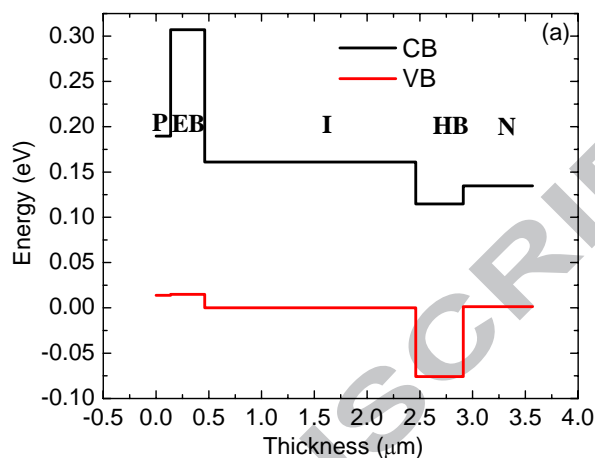


Figure 1(b)

50nm GaSb P+ contact (b) ($p = 2.8 \times 10^{18} \text{ cm}^{-3}$)
100nm EB $\text{Al}_{0.2}\text{Ga}_{0.8}\text{Sb}$
280P MW 10ML/10ML SLS (n.i.d.)
72P 16ML/7ML SLS ($n=3 \times 10^{18} \text{ cm}^{-3}$)
48P HB 13ML/4ML SLS (n.i.d.)
LW 14ML/7ML SLS (n.i.d.) 282 Periods
30P EB 8ML/8ML (n.i.d.)
94 Periods 13ML/8ML ($p = 2.8 \times 10^{18} \text{ cm}^{-3}$)
GaSb:Te

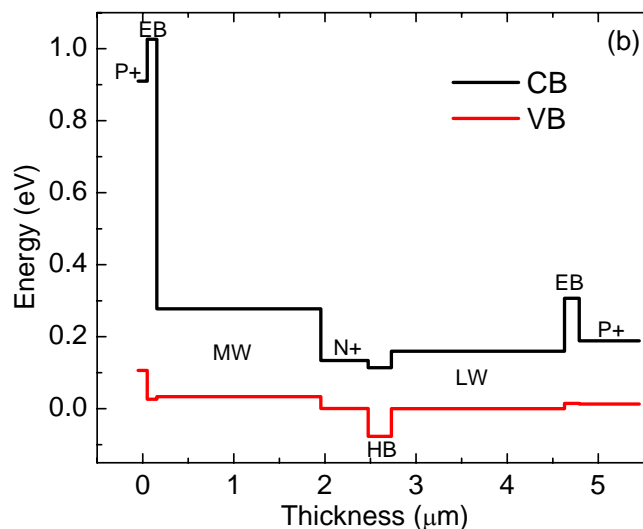


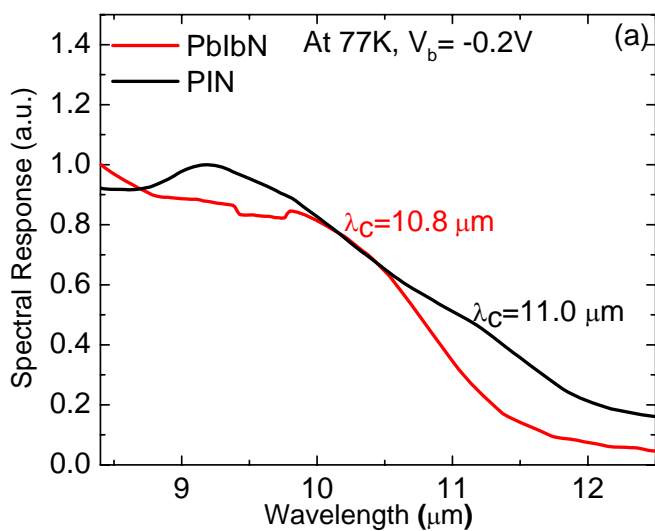
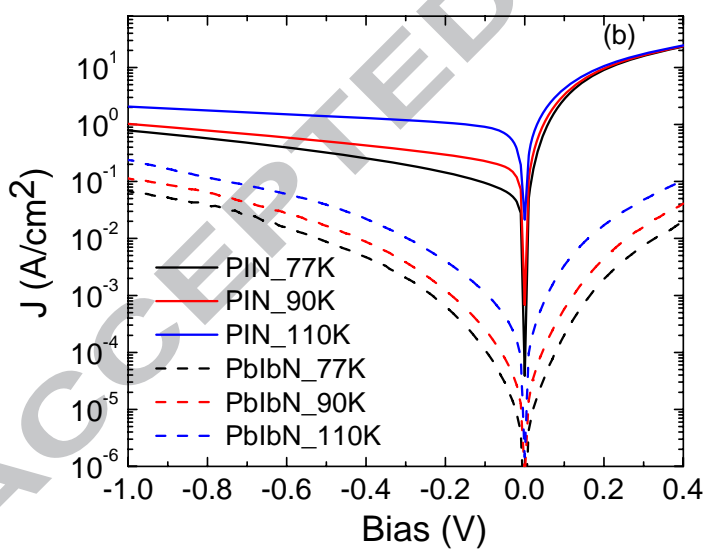
Figure 2(a)**Figure 2(b)**

Figure 3(a)

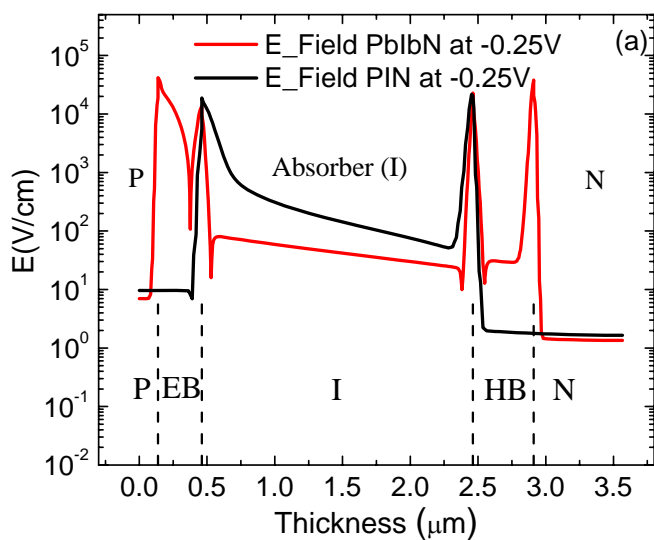
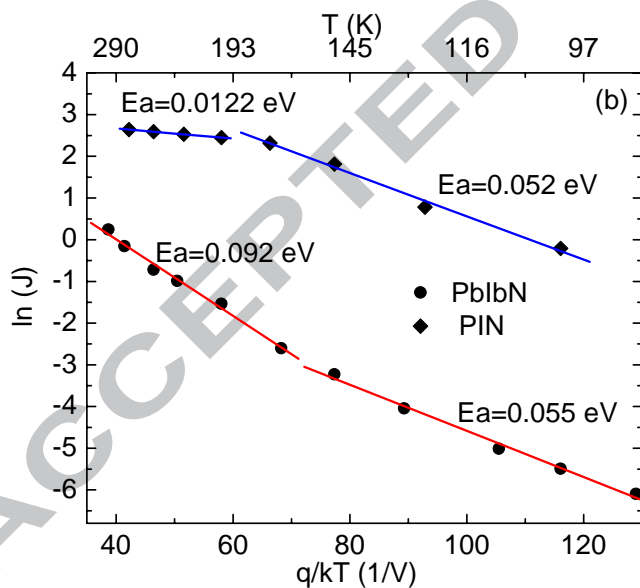


Figure 3(b)



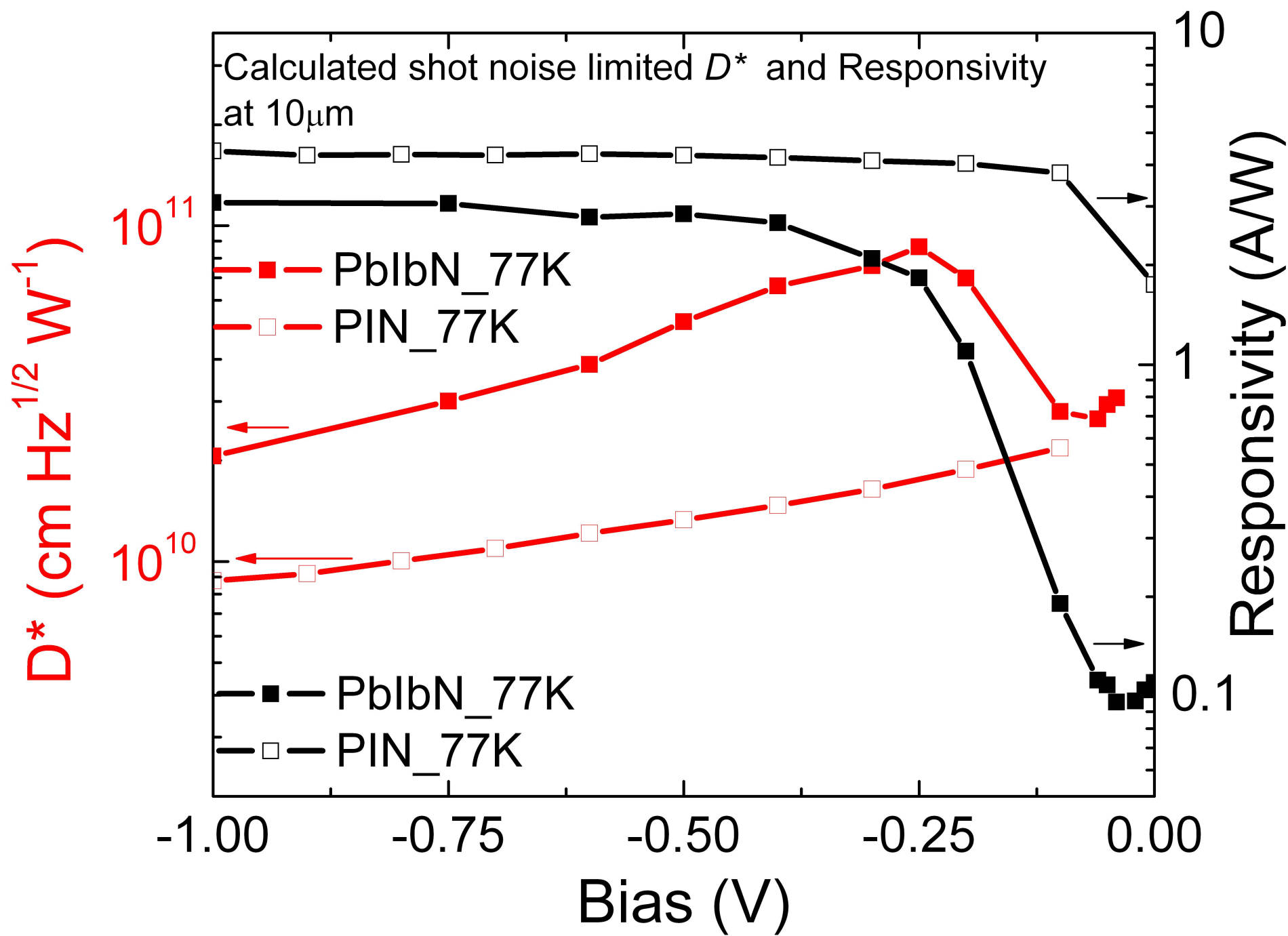
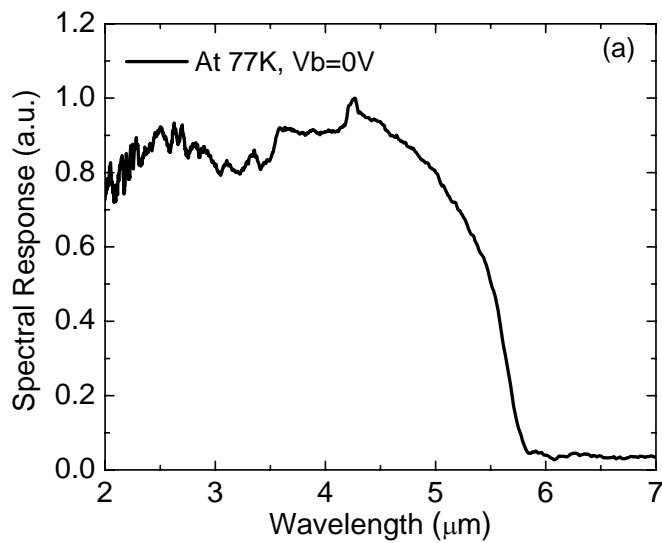


Figure 5(a)**Figure 5(b)**